Search for Fast Optical Transients Using Archival VERITAS Data

Gabriel Chernitsky

Master of Science

Department of Physics

McGill University

Montreal,Quebec

2017-4-12

Requirements Statement

ABSTRACT

Fast optical transient phenomena have been observed in the cosmos. Conventional optical telescopes typically lack the fine time resolution required to investigate sub-second transients. Ground based Cherenkov telescopes are powerful devices for finding optical transients as they are designed to capture optical light bursts on nanosecond time scales. The Very Energetic Radiation Imaging Telescope Array System (VERITAS) is an array of four imaging atmospheric Cherenkov telescopes (IACTs) that has been collecting data since 2007. A significant portion of the archived data corresponds to background signals that can be surveyed to find transient events. We discuss a methodology for conducting an archival search for serendipitous transients. With the analysis employed we achieved a nominal time resolution of approximately 150 ms and a limiting blue band magnitude of 8.9. The archival search revealed signals from transients occurring in the atmosphere, including meteor-like events and satellite flares. No astrophysical or astronomical candidates were found.

ABRÉGÉ

Des phénomnes de transmissions optiques rapides ont été observer dans le cosmos. Cependant, les télescopes optiques conventionnels n'ont pas la résolution temporelle suffisante pour observer des transmissions de moins dune seconde. Nous utilisons Les télescopes de Tcherenkov pour ce faire, ce sont des outils puissants pour trouver ces transmissions optiques. Ils peuvent capter des impulsions de transmission optique à léchelle de la nanoseconde. En fonction depuis 2007, VERITAS (Very Energetic Radiation Imaging Telescope Array System) est un réseau de 4 télescopes à imagerie Tcherenkov atmosphérique. Une grande partie des données darchive corresponde à des signaux de fond qui peuvent être examiner pour trouver événement de transmission optique. Dans cette thèse, nous développons une méthodologie pour trouver des transmissions optiques fortuite dans les archives. L'analyse utilise permet datteindre une résolution nominale temporelle dapproximativement 150 ms et d'une limite dans la bande B de magnitude 8.9. Les recherches dans les archives ont révélé des signaux des transmissions optiques ayant eu lieu dans l'atmosphre, cela inclut les météorites et les satellites. Aucun candidat astrophysique ou astronomique n'a été observer.

ACKNOWLEDGEMENTS

I would first like to thank my supervisor, Prof. David Hanna, for all his guidance and support while working on my thesis. The aid and insight that he has provided for me has helped me learn difficult concepts in physics as well as mathematics and perform research I once thought was insurmountable. I want to thank Prof. Kenneth Ragan as well for his advice and help in understanding the complex details of astroparticle physics. My thanks extends to the rest of the VERITAS group at McGill, Jonathan Tyler, Tony Lin, Samuel Trépanier, Qi Feng and Benjamin Zitzer as well as Étienne Bourbeau. I am thankful for all great conversations that were had with this group of excellent people. I would like to extend my thanks one more time to include the entire VERITAS collaboration. The members of VERITAS have been very helpful in teaching me the ropes, specially in my early days when I was a novice graduate student. Finally I would like to thank all my friends and family. If there has ever been a time where I forgot the importance and worth of my own work, they would be eager to remind me of how far I had come and how much I was accomplishing. If my research keeps my head in the sky, then their love and support keeps my feet on the ground.

CONTRIBUTIONS FROM THE AUTHOR

The purpose of this thesis is to highlight the capabilities of the VERITAS array in observing fast optical transients, as well as establishing and verifying a methodology for their search. Original contributions from the author are as follows:

- Chapter 3: Producing calibration curves that shows the telescope's response to starlight as a function of apparent B-band magnitude. Calculated the limiting sensitivity of a pixel based on its time resolution and binning. Also developed software that calls on SIMBAD and VERITAS databases to locate stars in the telescope's FOV during observations. The software is written in Python.
- Chapter 4: All results published in this chapter are from the author's own work. The data analysis that was done to find these results is based on already existing techniques found in literature.

Chapter 1 and 2 present information gathered from literature. Beyond this thesis, the author has helped the VERITAS collaboration by fulfilling observing shifts on-site. The author has also been responsible for reflectivity measurements as well as maintaining and updating the reflectivity analysis software.

TABLE OF CONTENTS

LIST OF TABLES

Table page

LIST OF FIGURES

CHAPTER 1
Transients

Events that last a limited amount of time are referred to as transients. In the early days of astronomy and astrophysics, transient observation was limited to optical transients that could be seen by the naked eye. Supernovae and meteors were the first transients seen, due to their brightness. As telescope technology developed, astronomers were able to identify optical phenomena that were fainter, had a brief time span and required a good angular resolution.

Further developments allowed observations of transient electromagnetic (EM) signals outside the visible range as well as fast signals lasting less than a second. Transients are often comprised of different types of EM radiation; for example a gamma-ray burst (GRB) has an afterglow comprising x-rays down to radio waves. It is not sufficient to study a transient by searching for signals in a specific domain, but rather it requires studying signals from all forms of radiation to fully understand the phenomenon. For the purpose of this thesis we will be discussing fast optical transients (FOTs) in the time scale of 10^{-3} to 10^{3} seconds.

1.1 Fast Optical Transients

FOTs are observed as a change in optical brightness from a region in the sky due to a sudden increase in the source luminosity (such as a stellar flare) or a decrease in the observed flux from the source (such as a stellar eclipse). The luminosity of these events is generally measured through bandpass filters that are transparent only to a narrow range of wavelengths.

We will classify FOTs produced outside the atmosphere as either astrophysical or astronomical transients. Events that primarily involve the movement of celestial bodies, such as eclipses, are astronomical transients. Events involving physical processes within a celestial body are astrophysical transients. Transient events occurring in the atmosphere are categorized as terrestrial transients. The reason for this distinction is that astrophysical and astronomical transients usually occupy a point-like region of the sky while terrestrial transients tend to move through the sky. A simple way to distinguish an astrophysical or astronomical transient from a terrestrial one is that terrestrial transients trail across the sky and are generally seen for a few seconds. What follows is a brief outline of various types of FOTs.

1.1.1 Astrophysical Transients

Novae

Novae are bright flares that occur when a white dwarf accretes a large amount of hydrogen-rich gas from a stellar companion in close orbit. The gas forms an atmosphere that is gradually heated by the core of the white dwarf. Eventually the hydrogen in the atmosphere is hot enough to undergo hydrogen burning and release large amounts of energy resulting in a nuclear explosion. The energy released from the explosion, or nova, pushes the accreted matter away from the white dwarf.

Nova explosions produce bright flares, with peak magnitudes reaching absolute magnitudes of -9 in the V-band, which is a filter with a bandpass centered at 550 nm [1]. The bright glow following a nova does not last more than a few days, after

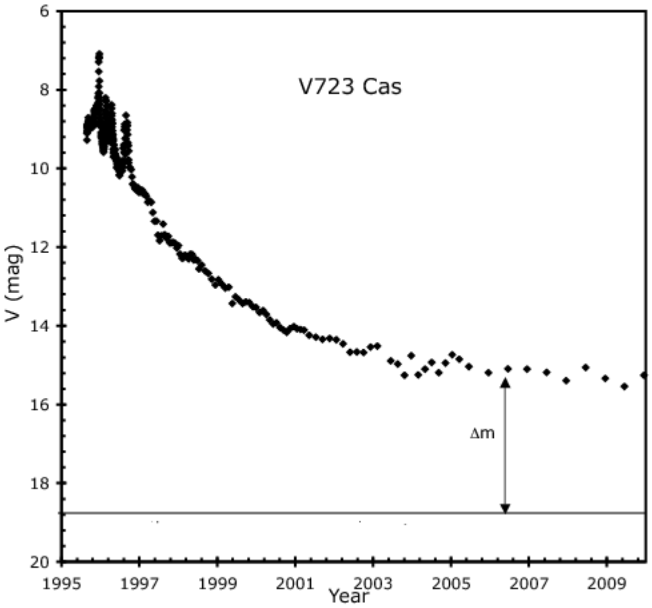

Figure 1–1: Light curve of nova V723 Cas produced from data in the AAVSO database. The database contains a large collection of images of V723 Cas, mainly by amateur astronomers, which are used to calculate the V-band magnitude of the nova. A line is drawn horizontally to show the pre-burst brightness of the source, δm is the difference in brightness across the nova eruption. Image source: figure 2 in [2].

reaching its peak magnitude the white dwarf begins to fade over the course of many years. A new nova can occur as long as the dwarf continues to accrete sufficient gas from the companion. Fig 1–1 shows the light curve of nova V723 Cas, measured from images collected by the American Association of Variable Star Observers (AAVSO).

Supernovae

Supernovae are violent flares that mark the death of a star. The first type of supernova, type Ia, follows a series of events similar to a nova: a white dwarf accreting matter from a companion. The amount of infalling matter provides a force of gravity too large to be balanced by radiative forces and the star begins to collapse. Temperatures rise and nuclear reactions re-commence at the core, unleashing a massive shockwave that ruptures the entire star.

Type II, or core collapse supernovae occur at the end of the life cycle of massive stars (masses of 8 $M_\odot$ and higher, where $M_\odot$ is the mass of the Sun). The stars reach a point in their cycle of nuclear reactions where the radiative output from fusion is lower than the gravitational pressure of the massive core. The core undergoes a collapse until the density reaches that of an atomic nucleus and it can not be compressed further. The sudden halt in compression produces a massive explosion, destroying the outer layers of the star and leaving behind a neutron star in place of the core. Supernova explosions result in really bright flares of V-band magnitudes -14 to -20 followed by a slow-decaying afterglow [1].

The intermediate Palomar Transient Factory (iPTF) is a leading survey in transient astronomy. iPTF, as well as its predecessor the Palomar Transient Factory (PTF) utilize a survey telescope. The telescope consists of a 8 deg^2 charge coupled device (CCD) camera installed on the 48-inch Oschin Schmidt Telescope in California [3]. CCDs are light sensors typically made up of millions of pixels, each made with photoelectric material to produce electrons from incident photons. The electron charge from each pixel is read out as a measure of the light reaching the CCDs over a set amount of time. The amount of time that a camera spends receiving photons before read-out is called exposure. With only a 60 second exposure the survey camera achieves an R-band sensitivity, which is centered at 658 nm, of 20.6 and is therefore sensitive to novae and supernovae. Follow up observations are performed by the

Palomar 60-Inch Telescope (P60). P60 has a 13” × 13” CCD camera and obtains a sensitivity of 23 after an hour-long exposure. PTF has developed a catalog of over 1000 supernovae, in Fig 1–2 we show four of them before and after the explosion.

GRB Afterglows

GRBs are extragalactic events that consist of a very energetic burst of gamma rays with measured fluxes of a few photons per cm^2 per second in the 50-300 keV range. GRBs have been associated with neutron stars merging together as well as hypernovas, a very energetic form of a supernova. The afterglow is produced from ejected particles interacting with gas [5]. Optical and X-ray afterglows following a GRB have been observed on multiple occasions [6]. Typically the optical afterglow is characterized by a seconds-long peak followed by a potentially slow fade period often lasting days or months. About 250 afterglows have been observed with a diverse range of apparent magnitudes, ranging from bright ($m_R = 5.5$) to very dim ($m_R = 28$).

One of the leading instruments in detection of GRBs and their afterglows is the Neil Gehrels *Swift* Observatory, or *Swift*, a satellite which has three telescopes on board [7]. The first is the Burst Alert Telescope which is sensitive to GRBs and triggers its other components when one is detected. The remaining components are the X-ray Telescope and the Ultra-violet/Optical telescope which monitor the GRB afterglow in the optical to X-ray range. *Swift* issues a GRB alert when it detects a burst so that other satellites and ground-based telescopes can observe the burst and its afterglow.

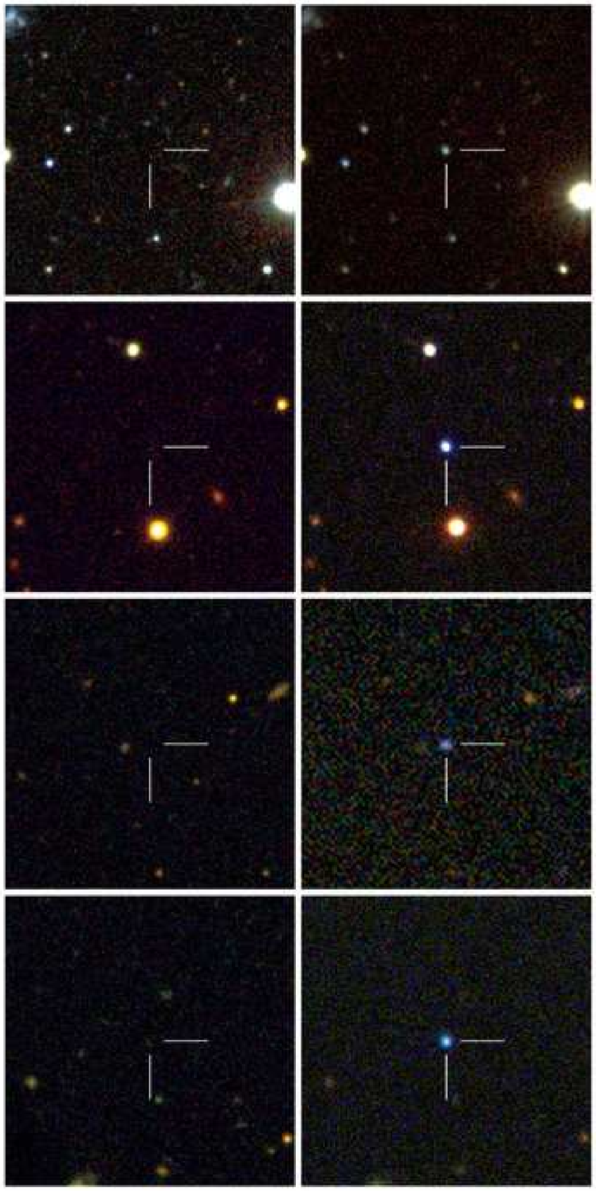

Figure 1–2: Photographs taken by Palomar Transient Factory's (PTF) 60-Inch telescope (P60) of four different supernovae before and after the explosion (left and right columns, respectively). The transients were first detected with PTF's survey telescope which triggers an alarm to which P60 can automatically respond within minutes. Image source: Palomar Observatory website [4].

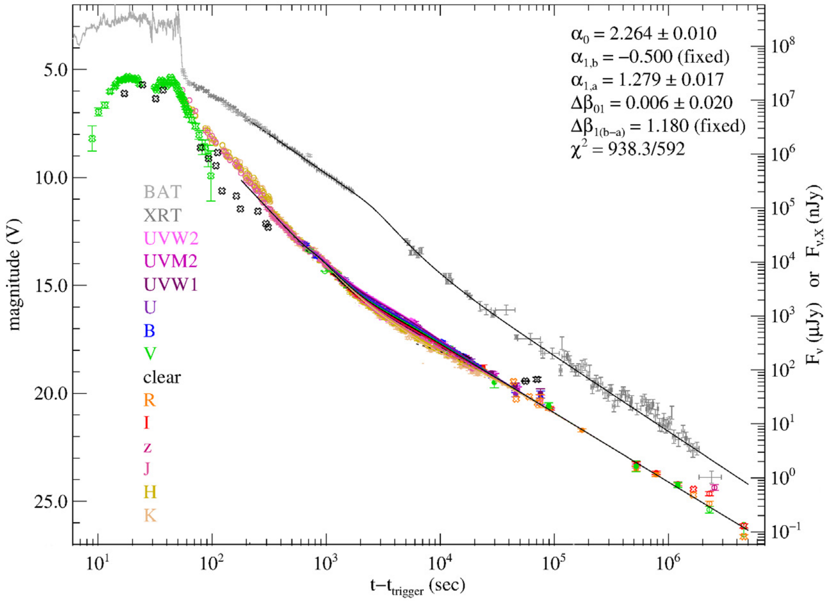

Figure 1–3: Light curve of the X-ray and optical afterglow of GRB 080319. The X-ray observations are shown in grey and were produced by *Swift*'s X-ray telescope. The bottom lightcurve is formed from observations done by various optical instruments including *Swift*'s own Ultra-violet/Optical telescope. The timescale is measured from the time that the *Swift* GRB trigger was set. Peak luminosity (≈ 5.5 in V band) is reached for about a minute. Image source: adapted from figure 1 in [8]. See image source for a detailed explanation of the data and variables.

Over 1000 GRBs have been observed by *Swift*; one of the best studied bursts is GRB 080319B which received lengthy follow-up observations of its bright after-glow (it reached a peak V-band luminosity of 5.5) [8]. The light curve produced from optical and X-ray observations of GRB 080319B shows a peak shortly after the GRB itself, followed by a slow fade lasting weeks (Fig 1–3).

Fast Radio Bursts

Fast radio bursts (FRBs) are, true to their name, millisecond duration bursts of radio waves. FRBs are a fairly new discovery in transient astronomy. The first FRB to be detected, called the Lorimer burst, was discovered in 2007 during a survey of archival data taken by the Parkes radio telescope in Australia (see [9] for more information).

Over 20 FRBs have been found, with similar characteristics. The observed peak flux density of these bursts is usually about one Jansky (Jy), with the exception of the Lorimer burst which reached 30 Jy. By comparison the radio pulses from the Crab pulsar have been observed to peak at 1500 Jy [10].

The radio signals that make up a burst have different frequencies. When a burst is detected the components of the signal appear dispersed in timing due to their interactions with electrons in the interstellar medium along their path of travel. The amount of dispersion seen can be used to approximate the distance to the source. FRBs have large dispersion measures, suggesting that their source is extragalactic. No repeat bursts have been found from the source locations, with only one exception. FRB121102 is the first known FRB with repeated instances of bursts in its original location. The first known burst was seen in 2012 and newer bursts were found occurring in 2015 (see [11] and [12]) and 2017 (see [13]). Multiwavelength observations of FRBs have been done with *Swift* and other instruments but no counterparts have been found.

There are various models found in the literature to explain the origin of an FRB. In [14] a model is discussed where FRBs are produced in powerful flares from a magnetar. A magnetar is a type of neutron star hosting a powerful magnetic field ($\approx 10^{15}$ G). As the magnetic field decays it causes bursts of gamma rays and X-rays. Magnetar flares could also cause prompt emission at other wavelengths including millisecond long optical transients with a stellar magnitude of 8.9 in the B-band which peaks at 445 nm. Optical telescopes can be used to monitor a region in the sky alongside a radio telescope to find an FRB with a coincident optical signal.

Flaring Red Dwarfs

Stars that undergo sudden increases in their luminosity for a short period of time are known as variable stars. One of the archetypical examples is Luyten 726-8B, or UV Ceti, a red dwarf close to the solar system characterized by its bright flaring activity. UV Ceti-like stars, which are variable red dwarfs (0.1 $M_\odot$ to 0.5 $M_\odot$), have characteristic flares on timescales of seconds to minutes [15]. Consecutive flares from a single star can have significantly different rise times as shown in Fig 1–4. Nominally UV Ceti-like stars are dim, with an average visual magnitude of 10 but during flares they can peak at magnitude 8 to 10 [16]. It is believed that flares occur due to magnetic reconnection in the stars' atmospheres similar to how solar flares are produced.

Low Mass X-Ray Binaries

Binary systems consisting of a compact star, either a neutron star or a black hole, with a low mass companion, such as a dwarf star, are classified as low mass X-ray binaries (LMXB). The compact star accretes matter from its companion. The infalling matter forms an accretion disk around the compact star while some of the matter falls further in towards the powerful gravitational well of the star. As matter falls inwards it emits bursts of energy primarily in the range of X-rays (hence being named 'X-ray binaries') as well as other EM radiation including flares of optical light. Optical flares have been observed in a few binaries, their duration ranged from about

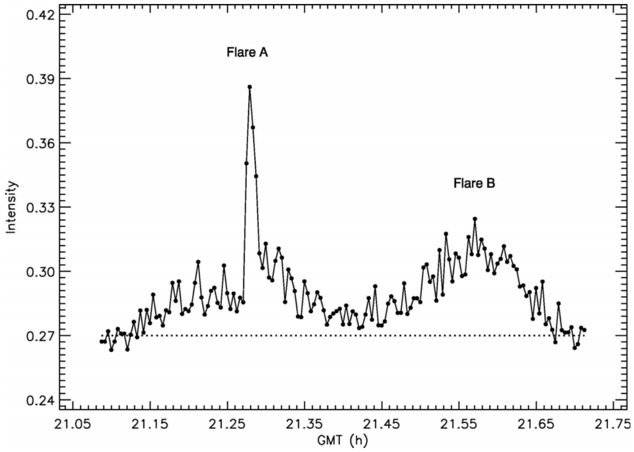

Figure 1–4: Light curve of EV Lac, a dim (M_V=10) red dwarf taken at the Ege University Observatory. The instrument used was a photometer attached to a Cassegrain telescope, reflecting light into photomultiplier tubes (PMTs). PMTs are devices that convert incident light to electronic signals. Two flares are observed: the first one lasts about 6 minutes while the second one is relatively dimmer and lasts about 15 minutes. Image source: figure 4 in [16]. The dotted line indicates the quiescent light level of the dwarf.

10^{-1} to 10^{2} ms [17]. The observed visual magnitudes varied from 19 to 16. There are about 150 known LMXBs in the Milky Way and more binaries are expected to be present in other galaxies such as M31 [18]. Optical follow-up observations of an X-ray source help determine if the source is an LMXB candidate.

1.1.2 Astronomical Transients

Microlensing and Exoplanet Searches

Microlensing occurs when a star is at least partially obscured by a compact object. The gravitational field of the foreground object acts as a lens, distorting the light of the background star causing it to appear brighter. This primary microlensing effect results in a rise in the apparent brightness observed and its timescale depends on the size of the lens. An exoplanet orbiting the foreground object, if properly aligned with the star, will create a secondary microlensing effect. The microlensing from the exoplanet causes a small peak in the light curve relative to the peak already produced from the primary microlensing. In Fig 1–5 we see a slow-varying rise from the main microlensing event with a deviation lasting a few hours caused by the presence of an exoplanet.

Jupiter-like exoplanets will cause a peak in the source's light curve lasting days while the effect from an Earth-mass planet lasts hours [20]. An eclipsing exoplanet can increase the apparent magnitude of the observed microlensing by 0.5. Exoplanets surveys look for secondary microlensing events in order to find exoplanets as they do not produce light and are too distant to be resolved.

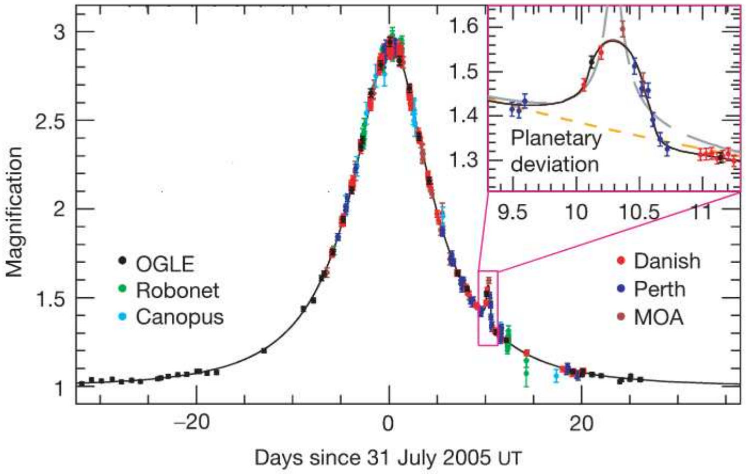

Figure 1–5: Light curve from a microlensing event as measured by various telescope experiments. Data points in the light curve are colored according to the instrument that made the particular measurement. The data values correspond to the magnification ratio between the observed flux and the quiescent flux of the background star. A fit is drawn as a black line across the data, The slow varying rise and fall in brightness is the result of a red dwarf magnifying the light of a star farther in the background as their orbits cross. The sudden deviation in the light curve (shown clearly in the inset), is caused by the presence of an exoplanet orbiting the dwarf and acting as a lens as well. These deviations last from hours to days and are characteristic to exoplanets which makes studying secondary microlensing a useful technique in their detection. In this example the devation lasted about 1.5 days. Image source: adapted from figure 1 in [19].

Stellar Occultations By Sub-Kilometric Objects

Transjovian Objects (TJOs) are objects in the solar system beyond Jupiter. Generally speaking they consist of asteroids, comets and minor planets. Occultations occur when an object moves between a celestial body and an observer. Kilometric TJOs are observed by the shadow they cast due to their occultation of a star, this would correspond to an observed dip in the star's light curve. Smaller objects spanning less than a kilometer cast a diffraction pattern instead that corresponds to a few short dips spanning a fraction of a second. The pattern is difficult to observe from the Earth as it moves quickly, at 30 km/s [21].

The three Fine Guidance Sensors (FGS) installed in the Hubble Space Telescope (HST) were able to detect a diffraction pattern on two separate occasions [22][23]. The FGS are interferometers built to keep the HST locked to a target by monitoring the position of nearby guide stars. PMTs in the FGS are read out 40 times per second [24]. Fig 1–6 shows the lightcurve of the occultation event, the peaks and troughs in the graph are caused by the diffraction pattern moving through the camera. The two occultation events found by the FGS were caused by objects located in the Kuiper belt just beyond the orbit of Neptune. Both objects were approximately 500 m in size.

1.1.3 Terrestrial Transients

Terrestrial transients are extended sources in a telescope's field of view (FOV) in contrast to astrophysical and astronomical transients which are produced by distant sources. Optical surveys looking for astrophysical transients such as GRB afterglows

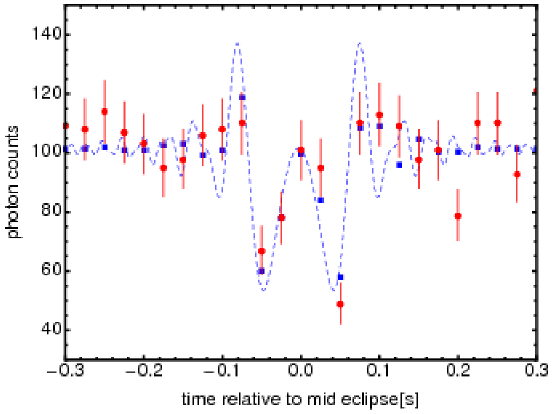

Figure 1–6: Light curve of a stellar occultation by a sub-kilometric object as produced from measurements taken by the Fine Guidance Sensors (FGS) onboard the Hubble Space Telescope (HST). Note the dips in the lightcurve near $t = 0$ separated by a short rise back to the baseline: this morphology is caused by the diffraction pattern emerging from the occultation. The blue points are simulated data and the red points are actual data points taken by a FGS at a rate of 40 Hz. Image source: Figure 5 in [23].

are subject to accidentally recording light caused by a bright meteor or aircraft in the night sky.

Comets and Meteors

Comets are objects a few kilometers in length, composed primarily of ice, hydrocarbons and silicates. They consist of a solid nucleus surrounded by an atmosphere of its own gaseous materials. Comets have long elliptical orbits around the Sun with periods ranging from a few years to over 200 years. When a comet is in orbit near Earth a trail of light can be seen, produced by the atmosphere of the comet. This observable transient appears fixed in the night sky as comets are millions of kilometers away from Earth. Comet trails can be observed for weeks until they become too dim to be seen.

Comets orbiting near the Sun are subject to strong bursts of evaporation. During evaporation small parts of the nucleus are stripped away, becoming dust particles in the solar system. These dust particles or meteoroids have a fairly uneventful lifespan until interacting with the atmosphere of a passing planet. When the Earth encounters a meteoroid it begins to fall through the atmosphere at speeds ranging from 10 to 100 km/s. Meteoroids usually disintegrate at altitudes of 100 km because of the friction generated by the surrounding air. The atoms on the surface of the meteoroid are ionized by collisions from air particles which in turn produces a bright flash of ionization light. Evaporated meteoroid particles can ionize the surrounding air. The ionized air subsequently produces a faint trail of light (Fig 1–7). The entire flash, referred to as a meteor or 'shooting star' lasts less than a second and can be seen by the naked eye. Most meteoroids are light, weighing less than a gram, which is sufficient to produce meteors reaching visual magnitudes of -8. Heavier meteoroids can produce spectacular bursts of light known as bolides or 'fireballs' that have been observed to reach magnitudes of -18 [25].

Satellites

Artificial satellites pace the Earth in orbits ranging from 160 to 200 km in low Earth orbit (LEO) up to geostationary Earth orbit (GEO) at altitudes of 36000 km. Some common components of satellites such as antennas and solar panels can reflect sunlight (or moonlight) towards the Earth. A satellite flare occurs when the rotation and position of a satellite results in it reflecting sunlight (or moonlight) onto the observer. Satellites appear as a constant trail of light in an image, or a relatively flat peak in a light-curve. Satellites move in slow orbits of 3-8 km/s; a 'flaring'

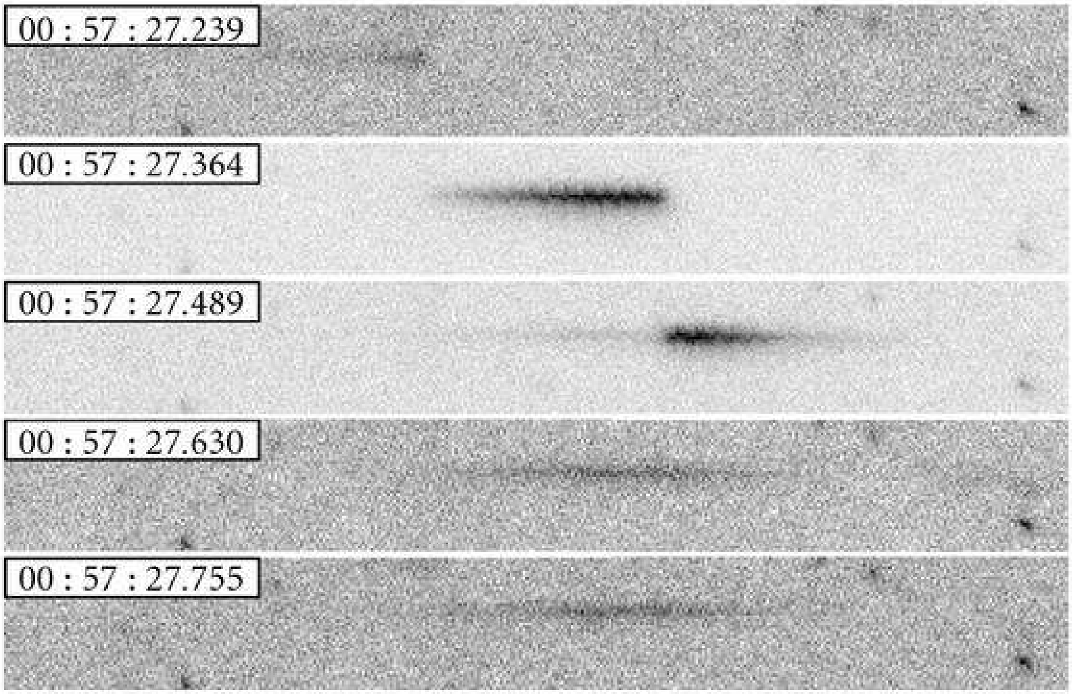

Figure 1–7: A meteor detected within a few frames taken by FAVOR, a wide-field CCD camera. Timestamps are shown in the upper-left corner of every frame. Meteor trails have variable signatures but they tend to consist of a fast burst (seen in the 2nd and 3rd frames from the top) followed by a dim afterglow produced from ionized gas (seen in the 4th and final frames). FAVOR has an exposure time of 0.13 s to achieve fine time resolution in observing astrophysical FOTs. This observation was serendipitous. Image source: figure 8 in [26].

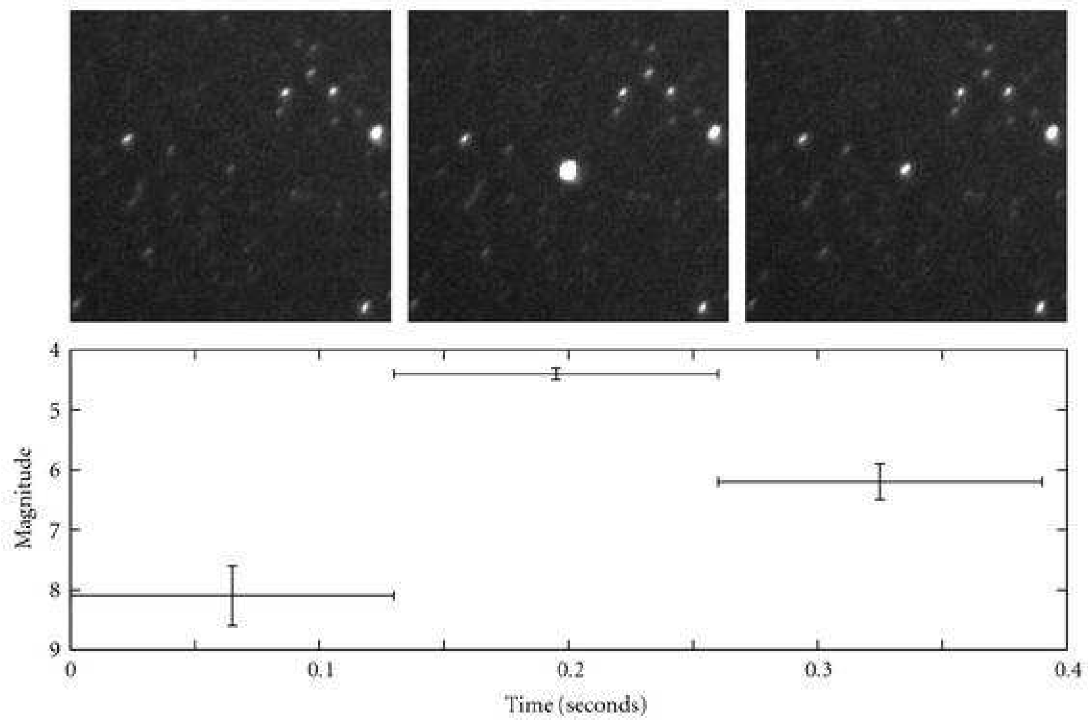

Figure 1–8: A satellite flare as seen by FAVOR across three frames with a lightcurve included. The flare peaks when most of the reflective part of the satellite faces the camera and diminishes as it rotates away. Image source: figure 7 in [26].

satellite can be observed for far longer than a meteor but eventually it fades as the reflective parts rotate away. We show a photograph of a short (0.3 s) satellite flare in Fig 1–8. The strongest satellite flares are produced by Iridium spacecrafts, a set of 66 communication satellites in LEO with reflective antennas causing flares that reach magnitude -8.

Aircraft

Air vehicles use lighting to make themselves visible in the sky. Aircraft passing through the FOV of an optical telescope will appear as a long line of light in an image, or a light curve slower than that of a meteor or satellite. Commercial airplanes fly at an altitude between 9 and 14 km. Aircraft and man-made satellites are not 'true' transients but it is worthwhile to consider how an optical telescope sees them and how their signal is distinct from a meteor.

1.2 Observing FOTs

In order to record light from the FOTs discussed above we must utilize a telescope with sub-second time resolution and fine sensitivity. Optical telescopes dedicated to transient searches rely on large FOVs to increase their chances of finding a transient. Historically these telescopes have employed CCD cameras with long exposures. CCD cameras offer arcsecond scale angular resolution thanks to the small size of their pixels. Consider the Palomar survey camera as an example: it uses an array of 12 CCDs. Each CCD consists of 8×10^6 pixels with a plate scale of 1 arcsec/pixel and they achieve an image with full width half maximum (FWHM) of 2 arcsec. The high sensitivity achieved by 60 second exposures allow Palomar to observe transients like GRB afterglows but with long exposure times faster transients like meteors are washed out in the data.

1.3 Atmospheric Cherenkov Telescopes

There is another type of optical telescope that is suitable for detecting transient signals. Imaging atmospheric Cherenkov telescopes (IACTs) are ground-based

Table 1–1: List of various optical telescopes including their FOV, time resolution and 5σ magnitude limit. Source: the second segment corresponds to Table 1 in [27], third segment is taken from [26], MAGIC parameters taken from [28].

Name	Field of view (deg^2)	Δt (s)	Limit (magnitudes)
VERITAS	$\sim$10	0.15	8.9^{m_B}
WIDGET	62 × 62	5	10^m
RAPTOR A/B	40 × 40	60	12^m
RAPTOR Q	180 × 180	10	10^m
BOOTES	16 × 11	30	12^m
pi of the sky	33 × 33	10	11.5^m
AROMA-W	25 × 25	5 - 100	10.5^m - 13^m
MASTER-VWF	20 × 21	5	11.5^m
MASTER-Net	30 × 30	1	9^m
FAVOR	16 × 24	0.13	10^m-11.5^m
TORTORA	24 × 32	0.13	9^m-10.5^m
Palomar	2 × 4	60	21^m
ROTSE-III	1.6 × 1.6	5	18.5^m
MAGIC-II Central PMT	0.1 × 1.6	1×10^{-3}	13.5^{m_U}

instruments designed to study gamma rays. Gamma rays interact with the atmosphere and produce an electromagnetic shower of particles. This extensive air shower consists of photons, electrons and positrons. The charged particles move at relativistic speeds which causes a burst of blue Cherenkov light in the surrounding air. A gamma-ray shower yields an overall burst of Cherenkov light lasting a few nanoseconds. IACTs collect this Cherenkov light using cameras equipped with PMTs and use it to determine the energy and direction of the primary gamma ray. Cherenkov light is faint so gamma ray observatories employ large reflecting dishes, about 10 meters or more in diameter, and multiple telescopes to increase their collecting areas. These telescopes also receive background light from ambient sources and starlight, generally referred to as night sky background (NSB). IACTs have fast integration times compared to optical telescopes but their PMTs offer poorer angular resolution compared to CCD pixels. The large size of PMTs is by design in order to have most of the Cherenkov light pool contained within a small fraction of the pixels in the camera.

1.3.1 Transient Searches With IACTs

There are three IACT arrays in operation: H.E.S.S , MAGIC and VERITAS. These instruments have been used in the past for optical surveys. An experiment in H.E.S.S saw the installation of a seven-pixel camera on the front cover of one telescope's Cherenkov cameras and investigated optical signals in X-ray binaries with a μs time resolution [29]. The MAGIC-II telescope has a parallel read-out chain for its central pixel designed to look for optical transients on timescales of milliseconds to seconds [28]. S. Griffin at McGill developed the VERITAS transient detector (VTD), a rate meter for VERITAS that can be connected to the constant-fraction-discriminators (CFD) of several PMTs in a single telescope [30]. The VTD samples CFD trigger counts at a maximum rate of 35 MHz which allows for measurements with microsecond time resolutions. J. Holder performed an archival search of VERITAS observation data to investigate the irregular light curve of star KIC 8462852 [31] with the hypothesis that the irregularities were caused by an artificial planet-sized structure eclipsing the star. The search did not find optical pulses from the star's region with duration longer than a few ns and blue-band magnitudes brighter than 6.4.

For the remainder of this thesis, we will discuss the ability of VERITAS to serendipitously detect fast optical transients. There are ten years worth of archival data consisting of over 10000 hours of observations. During a typical night the VERITAS cameras register a significant amount of uninteresting background but occasionally register signals from satellites and meteors (Fig 1–9) crossing the FOV. It is possible that other transients have been recorded as well. VERITAS has a coarse angular resolution (each pixel has a circular FOV of 0.15° in diameter) so it lacks the fine imaging capabilities of a CCD camera telescope. The advantages of VERITAS lie in the sensitivity offered by the large mirrored dishes and the fast temporal resolution of its PMTs and read-out electronics. Table 1–1 shows the FOV, minimum time resolutions and limiting magnitudes of VERITAS and various optical instruments.

We will conduct an archival search to study the background that VERITAS has recorded over time and develop a technique to identify transients. The advantage of archival searches is that they do not demand external hardware or dedicated observing times. The results and limitations of this archival search will help form the groundwork for future optical searches where time is alloted for observing regions where transient phenomena are expected.

Figure 1–9: A photograph of the sky taken shortly after sunset from the base of a VERITAS telescope during nightly operations. A light trail can be seen on the left part of the image. During the night many meteors, satellites, and air vehicles trail the skies. The light emanating from these objects can be recorded accidentally by the VERITAS cameras. Image source: Samuel Trépanier.

CHAPTER 2
VERITAS

VERITAS is an array of four IACTs. VERITAS (shown in Fig 2–1) is located in the basecamp of the the Fred Lawrence Whipple Observatory at the base of Mount Hopkins in southern Arizona, USA. The observatory is in latitude 31° 40' N, longitude 110° 52' W and altitude 1.3 km. The telescopes are positioned in a roughly square layout as shown in Fig 2–2.

Studying archived VERITAS data requires an understanding of the state of the experiment at the time of data-collection. The array has seen three significant developments since it began operations in 2007. There are three eras to the array, V4, V5 and V6, each one is begot by an upgrade. We choose to utilize data taken during the V5 era. V5 began when the layout of the array was finalized and it covers observations from September 2009 to July 2012. V5 offers a large collection of observational data to use thanks to its lifespan of nearly three years. The reason for choosing a past era instead of the current V6 is that the instrument, as used during V5, is better understood. In order to understand how VERITAS collects, measures and records optical light specially in the interest of observing transient phenomena, we dedicate this chapter to discussing the components of the telescopes present during the V5 era.

Figure 2–1: Picture of the VERITAS array at the Whipple Observatory. Image source: Larry Ciupik.

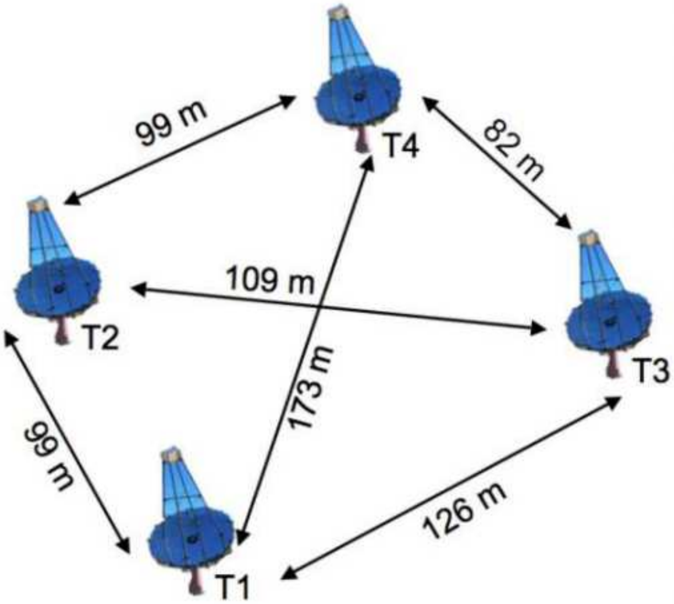

Figure 2–2: A schematic of the array highlighting the positions of each telescope as well as the inter-telescope distances. Image source: Roxanne Guenette.

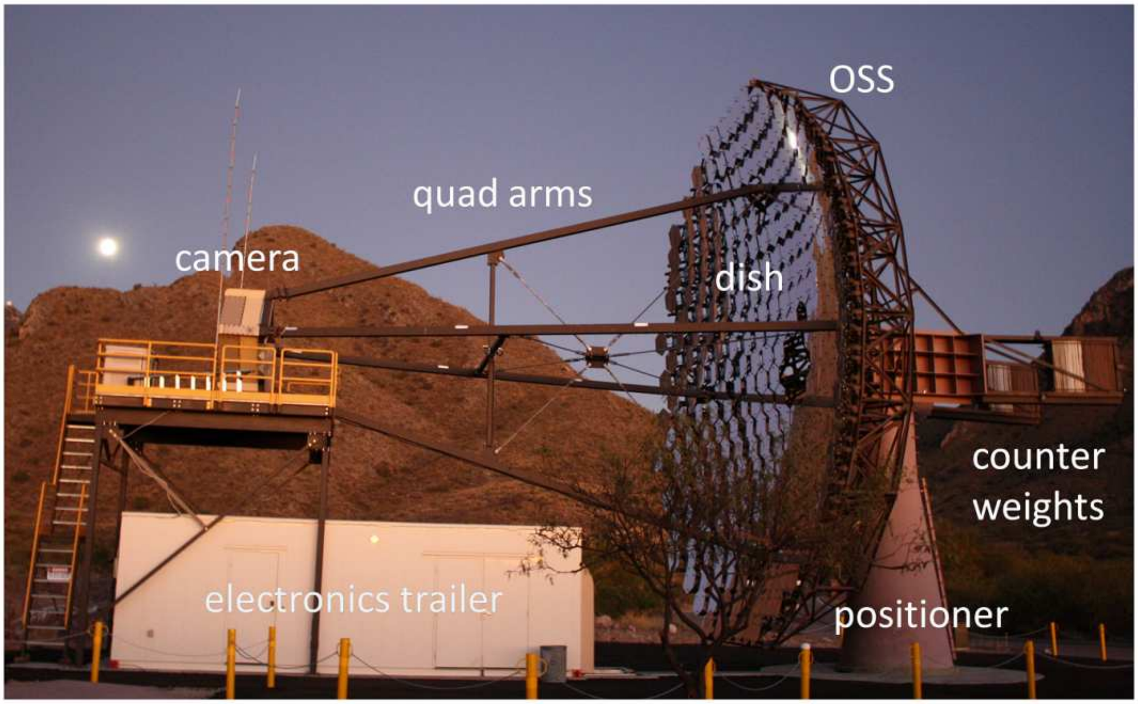

Figure 2–3: Photograph of Telescope 1 and the trailer hosting electronics. The main components of the telescope are labeled. Image source: Sean Griffin.

2.1 Telescope Components

A VERITAS telescope consists of a positioner base holding an optical-support-structure (OSS) which holds the remaining components. A photograph of Telescope 1 and its electronics trailer is shown in Fig 2–3. The first point of interest is the positioner and reflector.

2.2 Positioner and Reflector

The OSS is supported by an Azimuth-Elevation (Az-El) positioner that allows the telescope to be pointed anywhere in the sky above an elevation of 20°. The slewing speed is 1 deg/s and the pointing accuracy is approximately 50-100 arc seconds. The reflector, held by the OSS, consists of 345 identical hexagonal mirrored facets arranged in a Davies-Cotton design [32] and has a focal length of 12 meters. Each facet is mounted on its own three point base that allows it to be manually adjusted in all directions. The purpose of the reflector is to reflect Cherenkov light from air showers onto the camera placed at its focus.

2.3 Camera

The camera on each telescope is held by a quadropod extending from the OSS. The camera is housed in a metal box with a shutter on the front to protect the interior components from damage by daylight and adverse weather. The camera box holds 499 pixels in its interior. A pixel consists of a PMT that converts light received to electronic signals, a pre-amplifier device and an aluminum casing covering both components. A pixel with its components separated is shown in Fig 2–4. A single pixel has a circular field of view (FOV) with diameter 0.15° and the whole telescope camera has a FOV of 3.5°.

An array of light cones is fixed in front of the camera. Light cones help reduce dead-space between pixels and exclude light that was not from the reflectors. The light cones follow the design of a Winston light cone (see [33]) with the difference that the aperture has a hexagonal shape instead of being circular. In Fig 2–5 a camera is shown with the light cones in place. The most important components of the camera are the PMTs since they are responsible for detecting optical light.

2.3.1 PMTs

The PMTs are devices that take advantage of the photoelectric effect to turn incident light into an electric pulse. The photocathodes are sensitive to a broad range

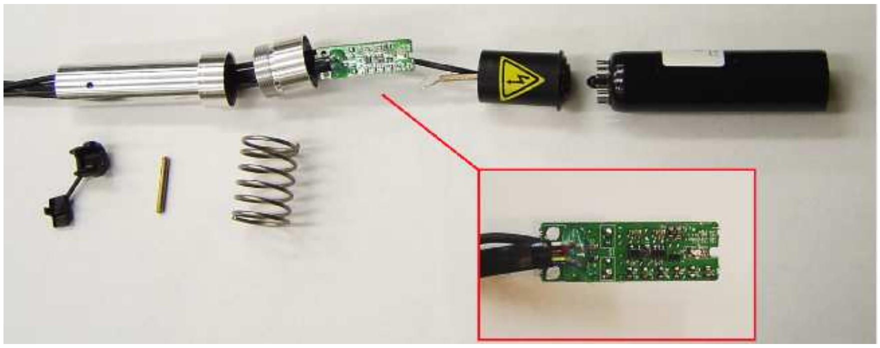

Figure 2–4: Picture of a disassembled pixel. The three main components are shown here from left to right: the aluminum casing, the pre-amplifier circuit and the PMT. The pre-amplifier circuit allows the anode current from the PMT to be monitored. Image source: figure 2 in [34].

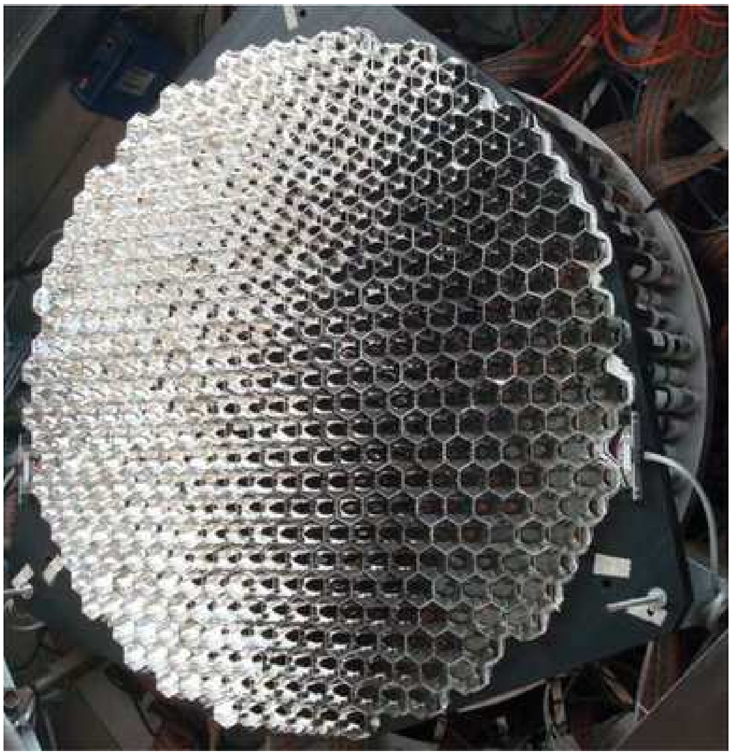

Figure 2–5: Telescope camera with the shutter open. The lightcones are deployed in front of the pixels. Image source: Sean Griffin.

of optical light. As shown in Fig 2–6 photons reaching the photocathode can eject a photoelectron that, driven by a high-voltage, will move to the first dynode. The photolectron is stopped at the dynode and knocks out a few electrons that proceed forwards to the next one. These ejected electrons stop at the second dynode and eject more electrons than what the original photoelectron ejected, effectively multiplying the charge moving through the PMT. The process repeats throughout the dynode chain, each step liberates more electrons and therefore multiplies the total charge that reaches the anode.

The cameras are equipped with Photonis XP 2970 PMTs. The quantum efficiency (QE), the probability that a photon ejects a photoelectron, is optimized so that it peaks in the range where the Cherenkov spectrum peaks as well (Fig 2–7). The QE is about 20% at 350 nm and the photoelectron collection efficiency is $\approx 75\%$ [35].

Attached to every PMT is a pre-amplifier circuit; The pre-amplifier increases the size of the PMT signal by a factor of 6.6. The PMT signal is AC-coupled before amplification. A secondary use of the pre-amplifier is measuring and monitoring the PMT anode current. Every pixel is attached to a 45 m coaxial cable. The cables carry electric signals out of the camera box, through the quadropod arms and positioner, and into a trailer holding read-out electronics that will digitize and store the signals.

2.3.2 Point Spread Function and Mirror Alignment

In order to calibrate the array's ability to image optical light it is necessary to quantify how the camera images a point source such as a star. The size of reflected light from a point source onto the camera is the point spread function (PSF). The

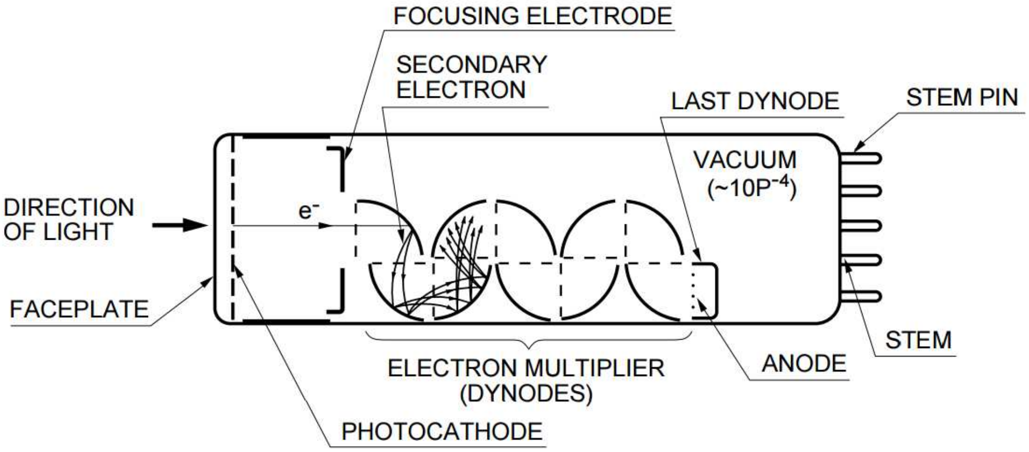

Figure 2–6: Diagram of a PMT highlighting its components. A photon enters through the faceplate and ejects a photoelectron from the photocathode which starts a cascade of electrons that reach an anode as a single pulse. Pulses exit the PMT as current. Image source: figure 2-1 in [36].

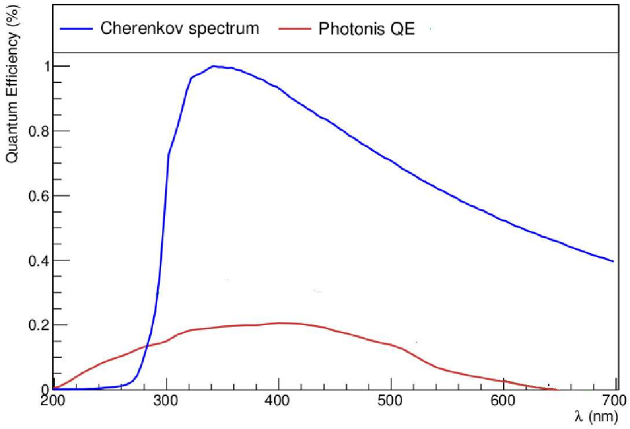

Figure 2–7: The QE of a Photonis PMT over the optical light range. The relative emission of Cherenkov light produced in a ∼500 GeV air shower is shown as well. The PMTs used by VERITAS are designed to be sensitive to the wavelengths where the Cherenkov spectrum peaks. Image source: adapted from figure 3-10 in [37].

PSF is calibrated so that it reaches a minimum of about 0.06° at telescope elevations of ∼60° as it is the typical elevation range during observations. The PSF increases with higher and lower elevations as the OSS bends under gravity.

Mirror alignments are performed to ensure every mirror facet is optimally aligned. The process involves a raster scan of a star to check how each mirror respond to starlight [38]. A properly aligned mirror will reflect the most starlight when the telescope is centered on the star. Mirror alignment guarantees that the PSF is sufficiently small that an image can be well contained within a single pixel (Fig 2–8). Two point sources can only be resolved if their separation is larger than the PSF; when observing celestial objects for transient signals we have to consider how light from nearby sources contributes to the image.

2.4 Data Acquisition and Read-out

The process in which PMT signals are digitized, filtered, and stored to a database is focused on storing signals from air showers and minimizing false alarms from NSB.

2.4.1 Flash Analog-to-Digital Converters

Incoming PMT signals reach the FADC (flash analog-to-digital converter) boards, installed in the trailers, that will measure the signals and output digital values. The signal arriving from a pixel is an electric current, the FADC measures the voltage produced by this current across a 75 Ω resistor. Every 2 ns the voltage is sampled and measured as a discrete value of digital counts. 8-bit samples are recorded at a rate of 500 MHz, each sample has a digital value ranging from 0 to 255. The reasoning behind choosing a 500 MHz sample rate is that a Cherenkov pulse lasts 4-8 ns, therefore the waveform has sufficient time resolution to sample the pulse over

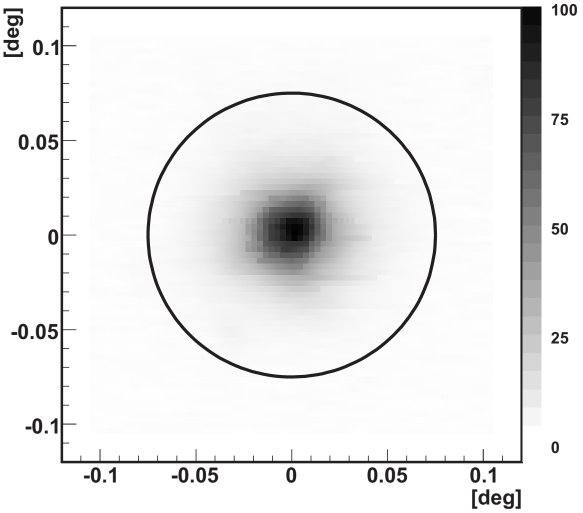

Figure 2–8: A photograph of the reflection of a star onto a plate set in front of the PMT camera of Telescope 4. The size of the image is determined by the point spread function (PSF) of the telescope. A circle is drawn around the image to show the angular size of a PMT. Note how the image is well contained inside the circle. Image source: figure 6 b in [38].

2-4 measurements. Cherenkov light seen by the FADC or an oscilloscope will have a large characteristic pulse in the waveform. A photograph of a single FADC board and a trace showing a typical Cherenkov pulse is shown in Fig 2–9. Every sample is stored in a 65 μs depth memory buffer.

Since each sample is a measurement of the voltage from electric signals, we can interpret the sample as a current measurement with Ohm's law (I = V/R where I is current, V is voltage and R is resistance). Integrating the current over a trace yields the charge output ($\int I dt = Q$) of the PMT during that time window. The charge is proportional to the gain of the PMT and the number of photoelectrons. The number of photoelectrons is proportional to the number of photons reaching the pixels. In other words, by digitizing the PMT signals produced by photons we are able to quantify the amount of light that the camera received over a discrete amount of time.

2.4.2 Trigger System

The frequency at which air showers occur is lower than the rate at which PMT pulses are digitized. The raw samples generated by the FADCs during operations are primarily populated by background. For the purpose of analyzing gamma-ray showers it is only necessary to store a set of samples (a trace) when some contain a Cherenkov pulse. A typical air shower has a light pattern that will strike all reflectors and illuminate a cluster of pixels in each camera. The read-out trigger system is designed to recognize the telescope's response to an air shower while minimizing false alarms from NSB. It is a three stage system operating at a pixel, telescope and array level.

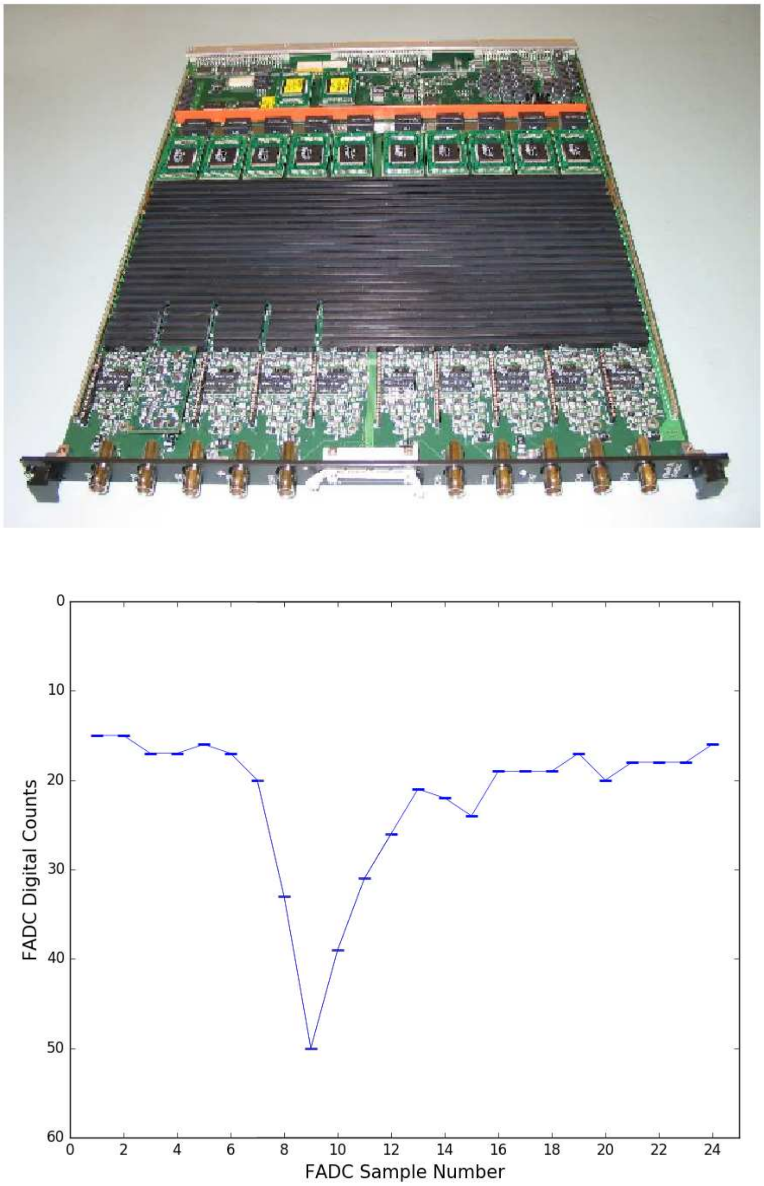

Figure 2–9: Top: photograph of an FADC board. The board has 10 input channels. Each channel connects a single pixel to a digitizer as well as a CFD. Bottom: Example of a typical FADC trace with a Cherenkov pulse. The trace is made up of multiple samples, in this case 24. Each sample is a voltage measurement taken every 2 ns. Air showers produce signals in the PMT that are seen as a pulse in the trace lasting only a few ns. Image source: VERITAS collaboration (top image).

L1-Pixel Trigger

The first trigger is a check on the analog pulse of each single pixel. Each FADC channel has a constant fraction discriminator (CFD), which is located on its board. A CFD receives signals in parallel with the digitizer. The CFD triggers when the pulse amplitude passes a set threshold. The threshold is calibrated so that pulses from air showers can trigger it but background light will not. Triggered CFD's send an L1 signal to the L2 trigger of the telescope that communicates signals from different pixels with each other.

L2-Telescope Trigger

The L2 trigger receives L1 signals and looks for coincident signals from a trio of pixels in a row or cluster. To register three signals as a L2 trigger they must coincide within a time window of 8 ns. A Cherenkov pulse reaches neighboring pixels almost simultaneously so the time window is narrow to avoid false alarms. In order to determine if multiple telescopes were triggered simultaneously, a third level trigger is employed.

L3-Array Trigger

The L3 computer, located by the control room, receives signals from the L2 boards in each telescope's trailer. The computer checks for L2 signals falling within a time window of 50 ns from at least two telescopes before issuing the final trigger. The pointing of the array causes light to arrive at the cameras with time offsets so variable time offsets are applied to the L2 signals to account for this. Another time offset occurs from the timing of L2 signals reaching the L3 as this varies depending on the cable length from one telescope to the L3. Built-in delays are set to account for the differences in timing.

2.4.3 Read-out

Once an array trigger is issued by the L3 computer it communicates to the Telescope Data Acquisition System (TDAQ) in every trailer that an event has occurred. The telescope Event Builder software looks back through the FADC memory buffer and reads out a 20 sample window (trace) corresponding to the pulse that set the trigger. The traces of every pixel along with trigger information including the timing of trigger are saved together as a telescope event and sent to the harvester. The harvester combines every telescope event into an array event and saves it to disk.

During read-out the FADCs will not record new measurements and electronics will not trigger and save a new event. This amounts to a deadtime, the time where the array is not measuring light, between one registered event and the next. The deadtime is kept low at approximately 15% so that during the time between events the telescope can trigger, reducing the chances that an air shower will occur during deadtime and not be recorded. At the conclusion of a run the array events are saved into a data file with a customized format known as a VERITAS bank format (vbf) file. All vbf files are sent to disks hosted by the University of California, Los Angeles (UCLA) where they can be accessed offline.

2.5 Hardware Monitors

VERITAS has multiple monitors to ensure that the hardware is running without issues. Hardware monitors measure real-time properties of the telescopes such as the high-voltage and current of the pixels, L2/L3 trigger rates, weather conditions, as well as the pointing of each telescope. Measurements from these monitors are saved to a database every minute. By querying the database a user can access archived data of a run which they would not otherwise find in its corresponding vbf file. For the purpose of this thesis we will highlight the current monitors and the sky camera.

2.5.1 Current Monitor

A set of 499 sensors, one for each pixel, is installed in each camera to continuously measure the current from the pixels. Current values are read out every second and are used during observations to observe the condition of the camera. PMTs are very sensitive: light from passing cars or even bright starlight can damage them so it is important to turn off the pixels when they face a bright source. The current monitor program checks that current in a pixel does not exceed 30 μA for over 4 seconds, if it does it will disable the high-voltage for that pixel.

2.5.2 Sky Camera

Each telescope is equipped with a pair of CCD cameras used for multiple purposes including measuring a telescope's PSF and determining the pointing of a telescope within an arc second using the position of stars as guides. The first camera, seen in Fig 2–10 is the 'sky camera' that is mounted on the lower quadropod arm and points in the same direction as the telescope. The FOV of each telescopes is monitored through the feed of their corresponding sky camera. Fig 2–10 (bottom) shows a photograph of the sky camera's FOV.

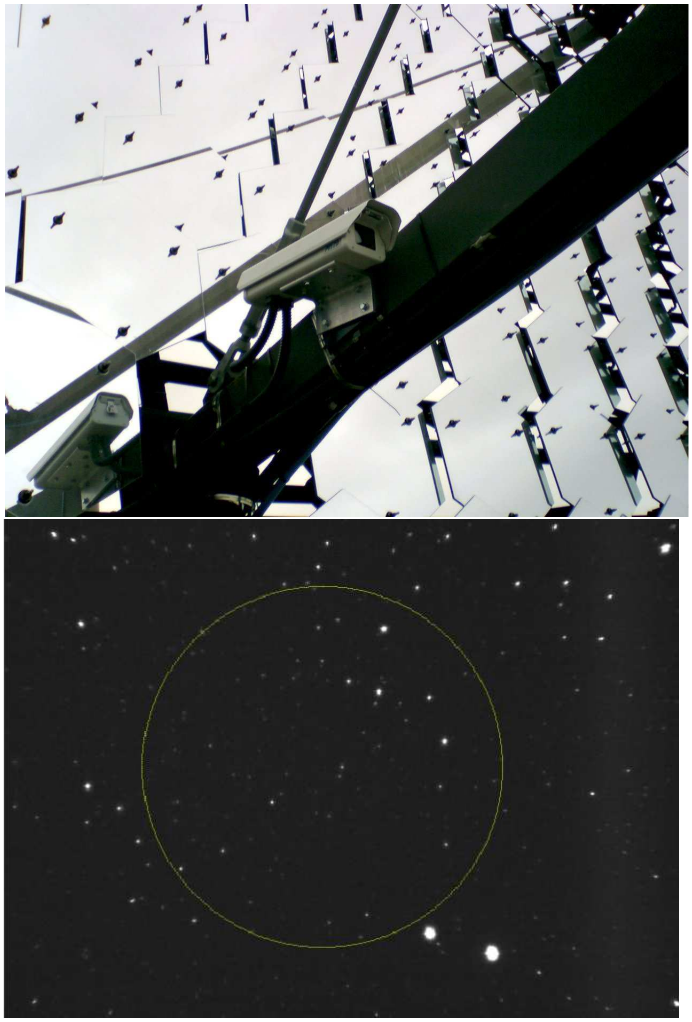

Figure 2–10: Top: A sky camera mounted on a quadropod arm of a telescope. The camera records the telescope pointing during operations and saves the information to a database. Some mirror facets are shown as well. Bottom: View from the sky camera set on Telescope 1 during an observing run. The circle bounds the FOV of the PMT camera. Image source: VERITAS Collaboration (top image).

CHAPTER 3
Methodology & Signal Analysis

Measurements taken during observations are used to study the optical light reaching the array. In order to use archival data to obtain a light curve that can be scanned for optical transients we must set a procedure that eliminates Cherenkov foreground, identifies pathologies and reduces noise from background fluctuations. The current measured from the pixels as well as their archived FADC traces can be used to measure light levels over the course of a run, as they are related to the light reaching the pixels.

3.1 Data Output and Acquisition

3.1.1 Read-out

When the L3 trigger registers an event, every FADC channel (one channel per pixel) read outs a trace of samples. A trace consists of 20 samples of digital counts as seen in Fig 3–1; samples are taken at 2 ns intervals. Over the course of a run FADC traces are read out from every channel at a rate of ∼200 Hz. Given that a typical run duration is 20 minutes, there is a large collection of stored traces per channel.

As discussed in the previous chapter the digital counts provide a measure of the photocurrent produced by incident photons on that pixel. A Cherenkov flash is registered as a signature pulse in the trace spanning a few samples. Traces lacking a Cherenkov pulse still show baseline fluctuations from NSB.

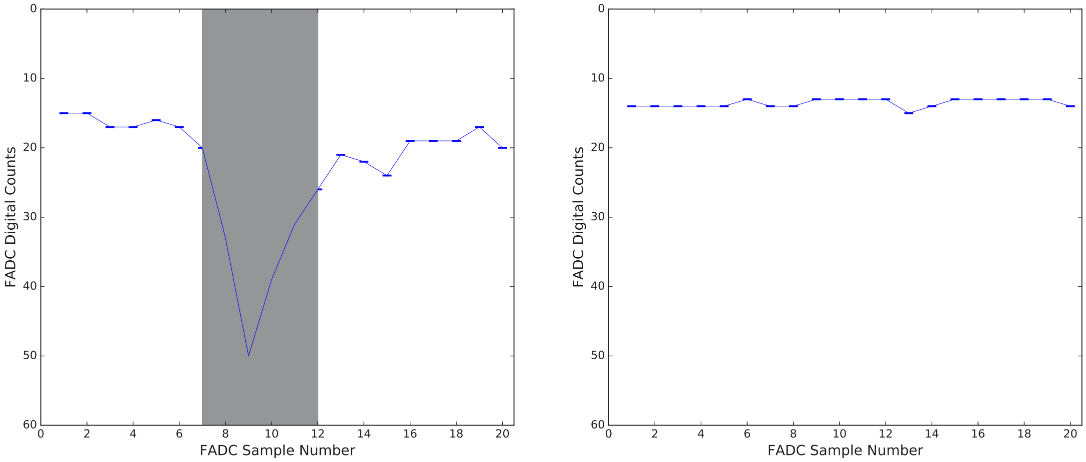

Figure 3–1: Example of an FADC trace from a single channel. Every trace is made up of 20 samples. Each sample is a measurement of the digitized signal taken every 2 ns. A line joining the samples is drawn to guide the eye. The large pulse on the left trace, highlighted in gray, is produced by Cherenkov light from an air shower. The right trace is relatively flat (a pedestal) and only produced by background.

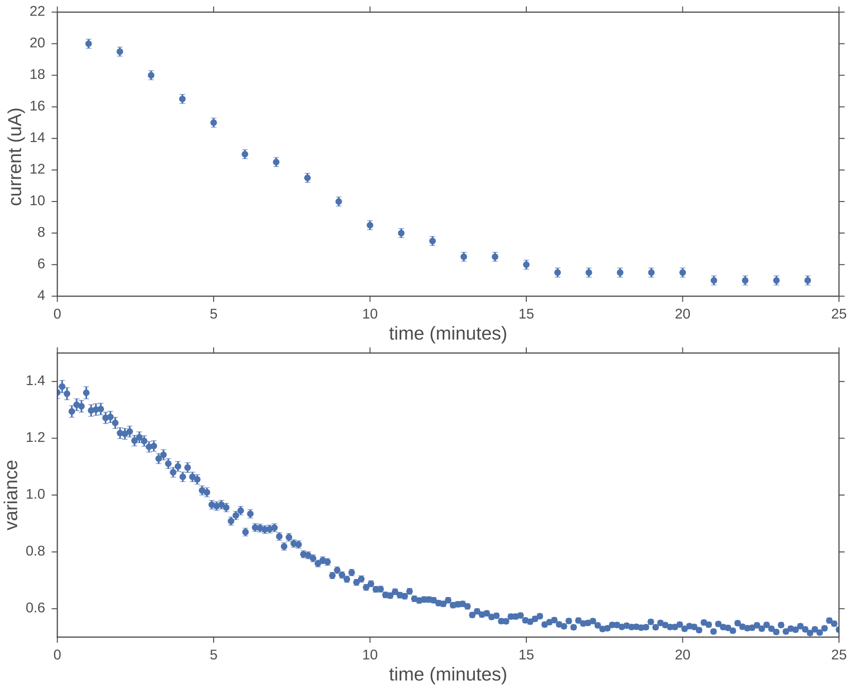

Figure 3–2: Top: current in a pixel over the duration of a single run. The values are samples from the current monitor which are only read out to the database once per minute. Bottom: same as above but using binned FADC trace variances with a bin width of 500 data points.

3.1.2 Current and Variance

The photocurrent through a pixel is measured every second with a current monitor attached to the PMT. Given that the Cherenkov light from air showers lasts a few ns the current samples are only correlated with the persistent background light. The measurements are done for monitoring purposes so they offer low resolution with a step size of 0.5 μA. Current samples are recorded to a database once per minute. While a lightcurve can be made using current as a proxy for light, it has coarse resolution and is insensitive to transients lasting less than a minute because the only stored current information are the minute samples.

An alternative is measuring the statistical variance of each individual FADC trace. We define the variance (σ^2) and error in the variance ($\delta\sigma^2$) of a trace with n samples as follows:

$$\sigma^2 = \frac{1}{n}\sum_{i=1}^{n}(x_i - \overline{x})^2, \tag{3.1}$$

$$\delta\sigma^2 = \sqrt{\frac{2}{n}}\sigma^2, \tag{3.2}$$

where x_i is the value of the i^{th} sample and $\overline{x}$ is the mean value of the samples.

It can be shown that there is a linear relationship between the variance of the samples in a trace and the current through the channel during that time span (for an analytic proof of this see [39]). This relationship allows the use of variances as a proxy for measuring the background light picked up by a PMT. Variances offer better time resolution than using archived current values because hundreds of traces are stored per second. We show current and variance compared over a single channel during a 25 minute exposure in Fig 3–2.

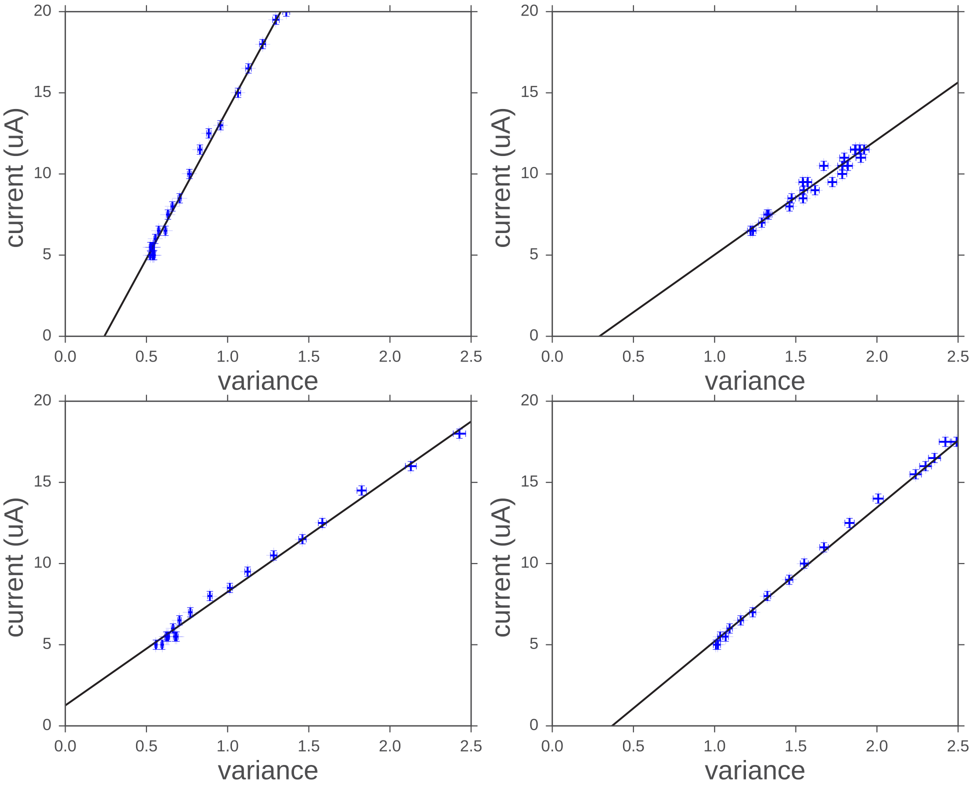

Figure 3–3: Correlation plot of variance and current for four different channels during the same run. The channel in the upper left is the one shown in Fig 3–2. Since there are more obtainable variances per minute than current samples, variance values in this graph are those whose timing is closest to the current sample.

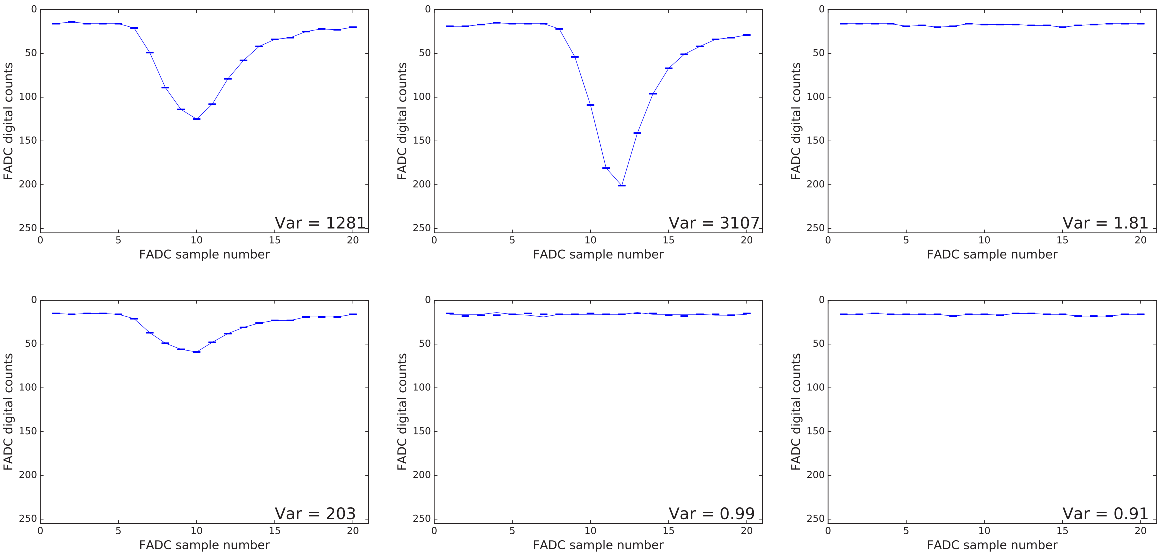

Figure 3–4: Example of various FADC traces and their variances. The first and second traces in the upper row, and the first trace in the bottom row contain a Cherenkov pulse. The variance in a trace is considerably smaller when it only comprises NSB fluctuations.

We obtained the variance of the traces that only contained background, divided them into sets of 500 and calculated the average value of each set. Every current sample was compared to the average variance from events occurring near the time the sample was taken. This empirical approach is based on the one found in [40]. As shown in Fig 3–3 there is a linear relationship between the variance of a trace and current; the relationship permits the use of variances as a measure of light. The intercepts of these graphs is not zero due to an unknown offset in each current monitor.

A proxy light curve can be made by obtaining the variance of every trace from a pixel and graphing them as a function of time. A trace with a Cherenkov pulse yields a much higher variance than one without. For the purpose of investigating light from a transient the variances due to the Cherenkov foreground are removed. During an event all channels are read out including those not receiving Cherenkov light, hence each channel will output traces whose variance indicates the level of background light which we use for a transient search. A sample set of traces taken from a single channel is shown in Fig 3–4 with their variances listed.

3.2 Signal Cuts

3.2.1 Removing Cherenkov Foreground

Once obtaining a run's worth of traces we proceed to applying a median cut in order to reduce Cherenkov light traces. All traces of a channel are obtained and have their variance calculated. Comparing the variances over the event number (as a proxy for time) of the run show that the distribution is biased towards events with background light while those with Cherenkov pulses form a tail at the high end of the distribution (see Fig 3–5 top).

Median Cut

The first step in removing the Cherenkov foreground and preserving the background is applying a median cut. The traces are grouped into sets of three and only the median in each set is kept. Cherenkov variances are infrequent outliers in a single channel because only 10% of the pixels are struck per event so its read-out will primarily be background; in a set of three consecutive variances is it unlikely that more than one variance will be foreground. The effects of a median cut in a distribution of variances is shown in the middle graph of Fig 3–5. Note that the tail in the higher end of the distribution caused by Cherenkov pulses is reduced and the distribution becomes narrower and more symmetric but is not yet Gaussian.

An alternative method to remove high variances would be to remove variances above a threshold. The threshold has to be set to remove Cherenkov variances without extinguishing variances caused by transients. The value of the Cherenkov variances vary depending on the channel as each set of variances has different baselines; a threshold would have to be chosen for each channel separately. The issue is that setting a threshold is biased and also subjective to each light curve. The median cut technique does not require calibration for separate light curves as it is based on how the variances are distributed rather than their value.

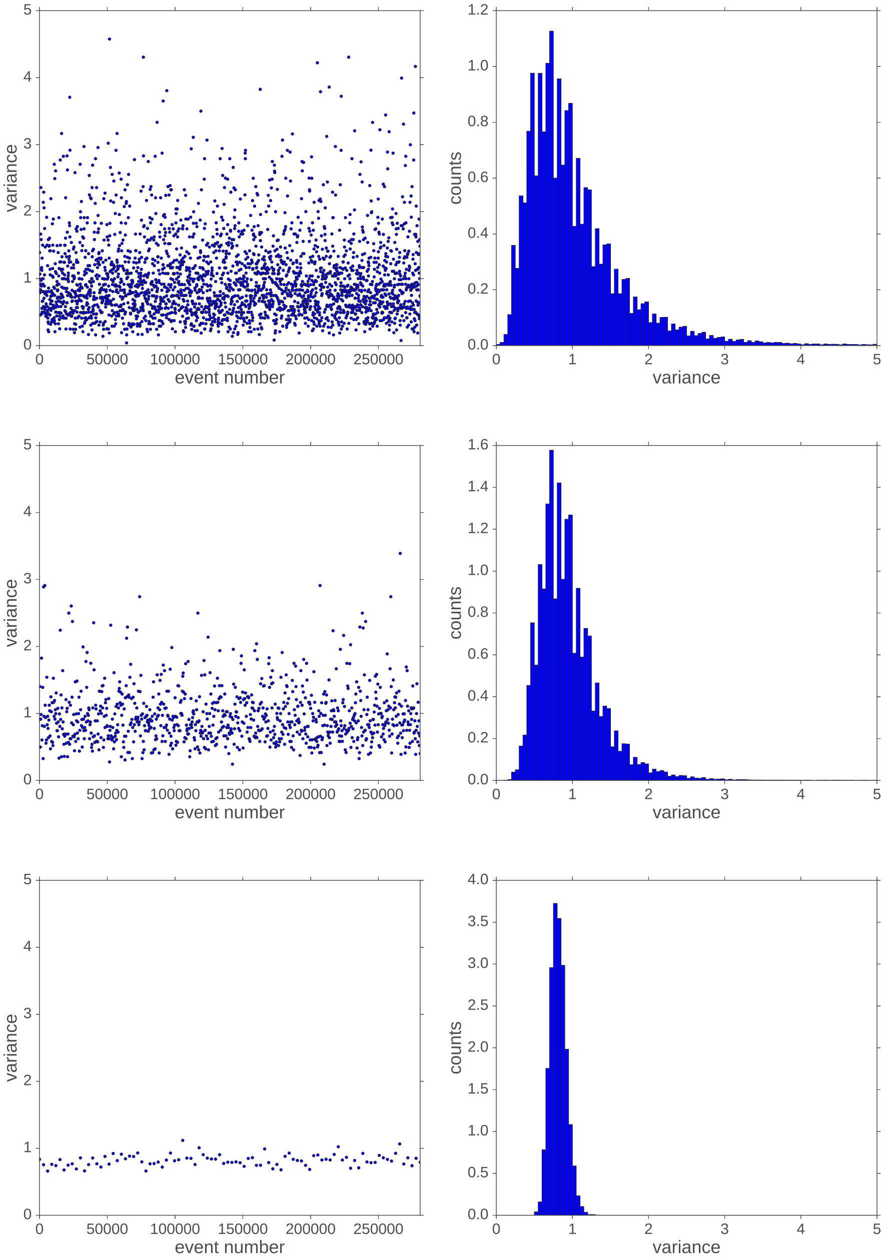

Figure 3–5: Graphs of variances vs event number. Top: variances from every trace in a single channel. Middle: variances after applying median cuts. Bottom: variances after applying median cuts and a profiling where only the lowest 80 percent of the variances in a bin of 10 were used to calculate the bin's value.

Profile

After applying the median cut some of the Cherenkov foreground remains and there are fluctuations in the baseline from NSB. We apply a profiling procedure in which the variances are binned and the value of each bin is the average of the lowest 80% of the bins entries. The mean value of a bin (σ_μ^2) and its uncertainty ($\delta\sigma_\mu^2$) are calculated as follows:

$$\sigma_\mu^2 = \frac{\sum_{i=1}^{N} 1/\sigma_i^2}{\sum_{i=1}^{N} 1/(\sigma_i^2)^2}, \tag{3.3}$$

$$\delta\sigma_\mu^2 = \sqrt{\frac{2}{n\sum_{i=1}^{N} 1/(\sigma_i^2)^2}}, \tag{3.4}$$

where σ_i^2 is the i^{th} variance in the bin, n is the number of samples in trace, and N is the number of variances used to calculate the average. The formulas for σ_μ^2 and its uncertainty are derived in appendix A.

Averages are taken to reduce the fluctuations in NSB variances as well as reduce the chances of a false alarm transient detection. By ignoring high value variances in the binning we ensure that outlying variances, such as those corresponding to a trace with a Cherenkov pulse, will not be accounted in the binning and that the bins value represents the background variances. The bottom graph of Fig 3–5 shows the result of cleaning the variances with the median cuts and profiling, the tail from Cherenkov pulses is not present. The clean variances act as a proxy light curve for background light reaching the pixels.

3.3 Time Resolution

The application of a median cut followed by a binning procedure (the profile) increase the minimum time width, Δt for detection of transients. Median cuts remove two thirds of the events and the time width increases by three. Profiling increases Δt by a factor of the bin width. For median-cut variances profiled into bins of 10, Δt = 150 ms assuming an average L3 rate of 200 Hz.

As the time width increases large fluctuations in the variance are smoothed over. The smoothing effect results in potential transient candidates being dismissed from the proxy light curve if the time span of the transient event is shorter than the bin size and time width. In Fig 3–6 we see a rise in variance lasting about a half second, likely due to a meteor moving across the FOV. With a bin size of 10 (top graph) the signature of a fast bright object is clearly noticeable as its approximate duration is larger than 0.15 s.

As we increase the bin size by a factor of 2 (middle graph) and 10 (bottom graph) the peak becomes indistinguishable from baseline fluctuations. The timescale used in this figure is obtained by converting the bin number to an average event number and that event divided by the average L3 rate of the entire run. The average L3 rate fluctuates throughout the run but generally it does not deviate significantly and thus we can use it to obtain an approximate timescale. Obtaining a precise timescale is left for the final stage of the analysis (see section 4.7).

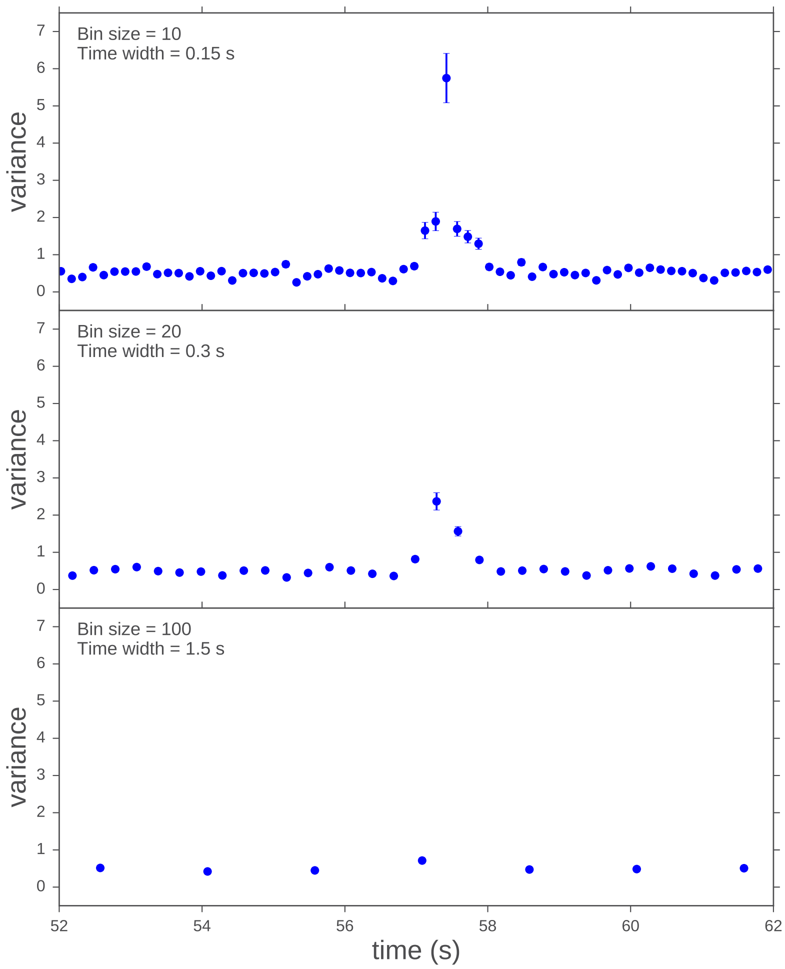

Figure 3–6: Light curves for a run with a transient. Note that the shape of the transient pulse becomes significantly flatter as the bin size is increased. The timescale is obtained by obtaining an approximate event number for each bin number and then converting the event number to a time using the average L3 rate.

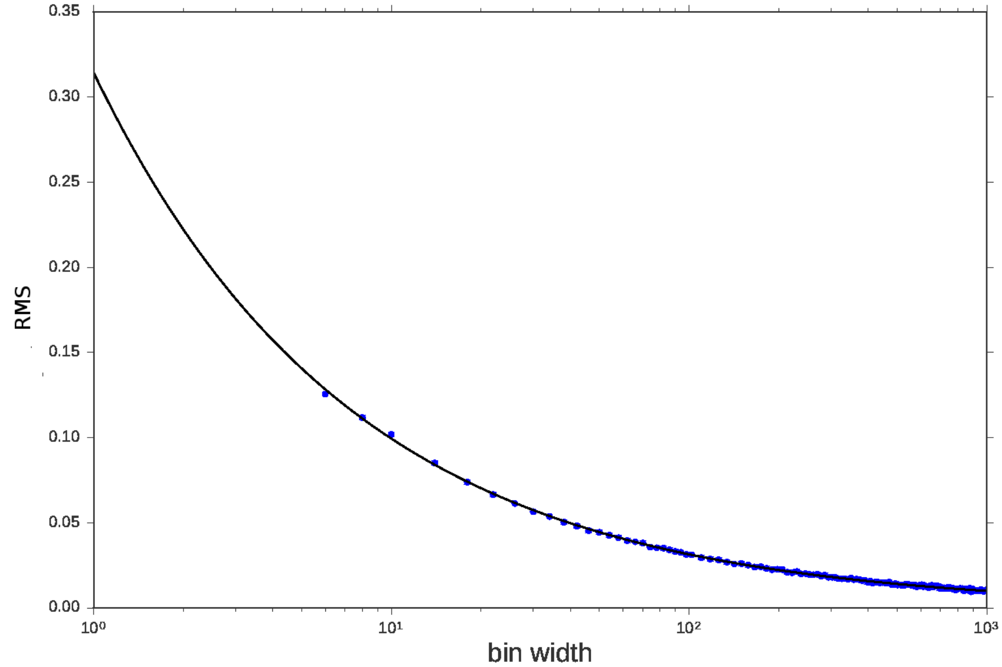

Figure 3–7: For a given bin width we show the root mean square (rms) of the distribution of variances in the light curve. A fit is done to the curves, corresponding to a inverse square root relationship between the bin size and the spread of the distribution which is expected if the distribution of variances is Gaussian.

For a given light curve consisting of profiled variance bins, we can quantify the 'smoothing' effect by measuring the root mean square (rms) of the data points for a particular bin width. This is motivated by the assumption that the background variances follow a Gaussian distribution. According to Gaussian statistics we expect an inverse square root relationship between the size of a bin and the rms of the variances. The correlation is obtained by calculating the rms of variances at various bin sizes and fitting the points to a function which is shown in Fig 3–7.

3.4 Removing Slow-Varying Trends

Once the cuts and binning have been applied to a channel's light curve, those channels without star effects or with zero current (discussed in section 3.6 and 3.7) proceed to a detrending process. Detrending is a technique that removes slowly varying fluctuations in the light curves. Every bin is subtracted by the median of 20 neighboring entries (10 entries before and 10 after the bin). Bins without all 20 'neighbors' (the first and last 10 bins in a light curve) are simply removed, these outliers are the first and last 10 bins in the light curve. An example of a typical light curve before and after the process is shown in Fig 3–8.

Detrending has the advantage that it removes trends in the variance such as increasing/decreasing NSB (ie during runs taken near sunset/sunrise) or the effect of some stars without eliminating shorter signals. As a more explicit example we show a curve with a brief peak in variance before and after the process (Fig 3–9); the steady increase in variance is removed but the peak remains.

3.5 Transient Trigger

Once the variances have been detrended, we require a trigger that can identify fluctuations in the variance. For the purpose of the archival search performed in this thesis we used a trigger that is set by peaks in the variance. For the light curve of any channel used in the analysis, the algorithm will trigger when there are three consecutive data points above 3σ from the baseline. Fig 3–10 has an example of a channel that the algorithm will trigger on. Information such as the run date, number, channel number, bin number and value of highest variance in the peak, is saved to a log. An approximate event number (by multiplying the bin number by the amount of

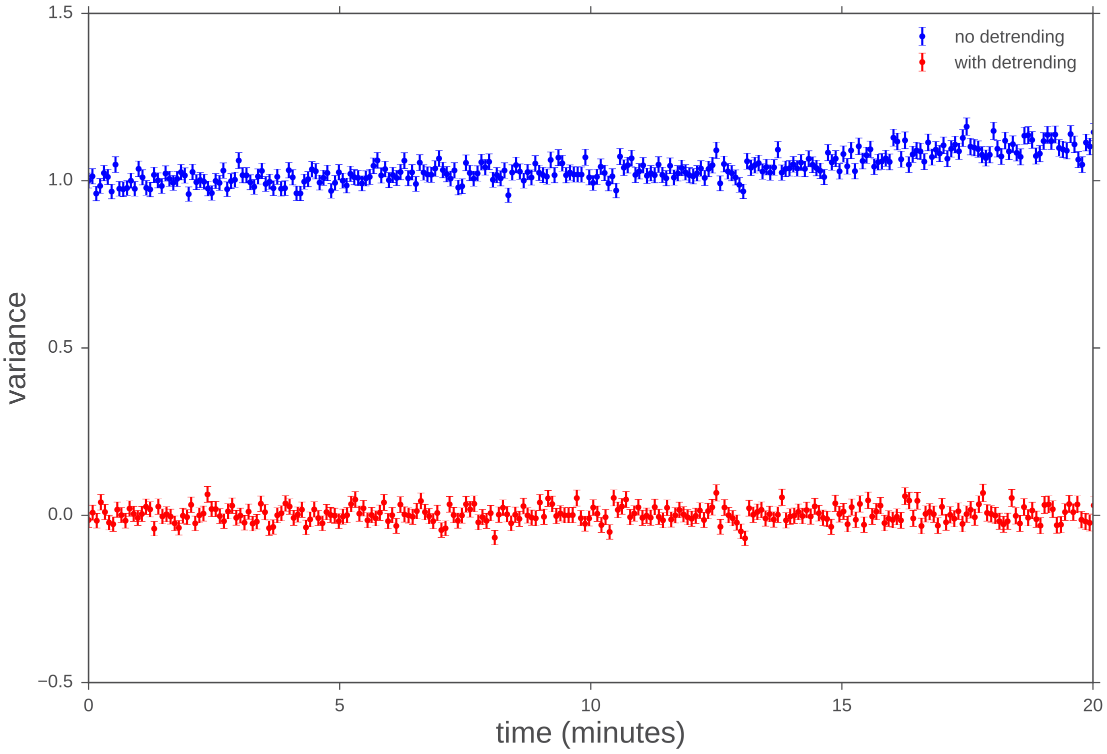

Figure 3–8: A lightcurve (blue) using bins of 500 variances is shown alongside its detrended version (red). The slow rise in variance towards the end is removed after detrending while the bin-to-bin noise remains intact.

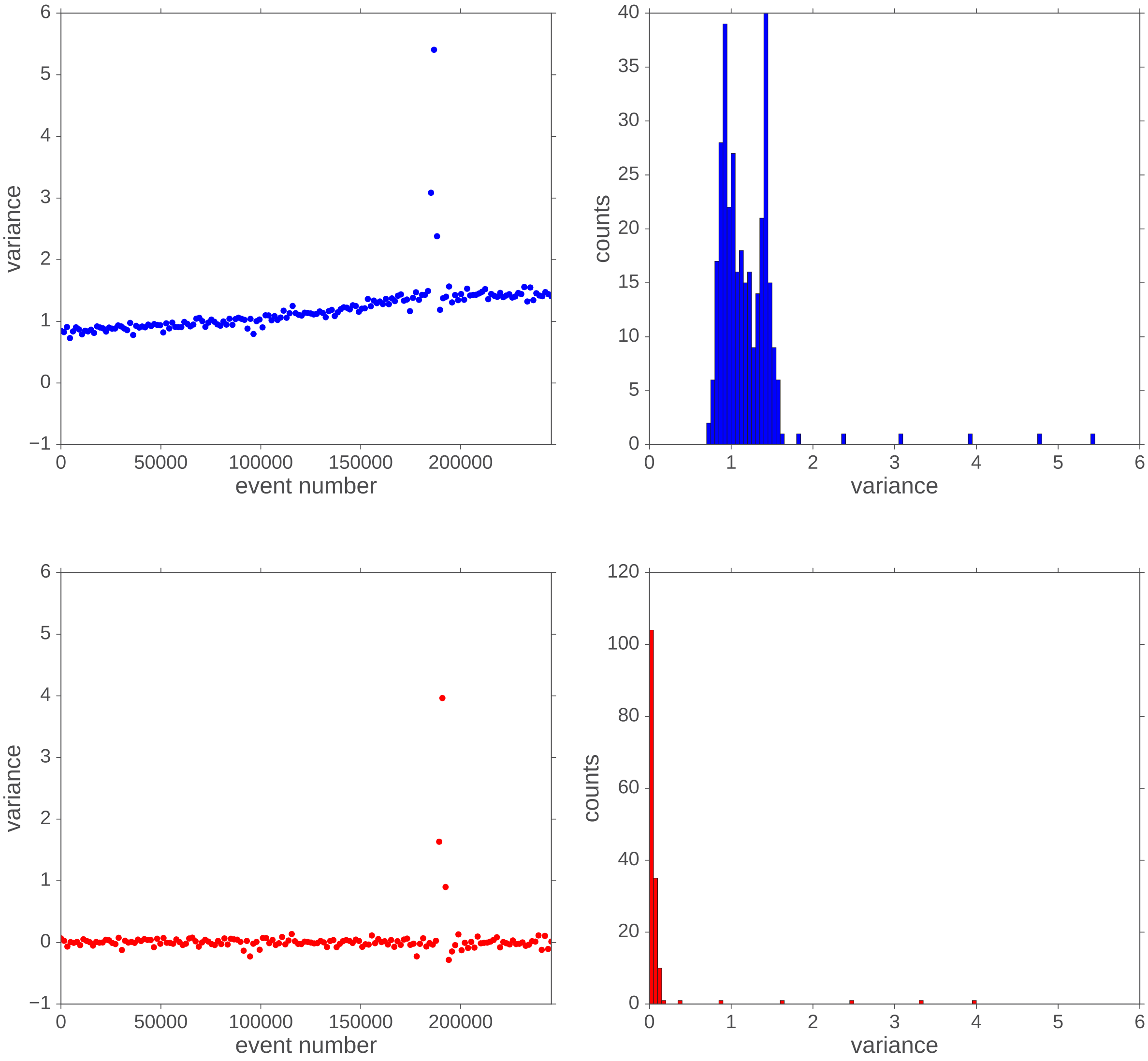

Figure 3–9: Top: variances post-profiling (with bin width of 500) and a histogram of the distribution. Bottom: as above but with the detrending process applied. The resulting variance lacks the slow-increasing trend but keeps the sharp peak lasting only a few bins.

variances per bin as well as a factor of 3 due to the median cut) and an approximate time (simply the approximate bin number times the average L3 rate) of the event are saved as well. The time values at this point in the analysis are not meant to be an accurate recording of the 'time of night' when a transient occurred but simply an estimate; the trigger algorithm is oblivious to the timing of the bins.

3.6 Primary Transient Analysis

The primary analysis is done on a single-run basis. In preparation for the analysis the vbf file for the run is obtained from the UCLA servers and all its FADC traces in a particular telescope are extracted. vbf files occupy a few GB of memory so to conserve disk space the variance of every trace in every channel is calculated and then saved to a Hierarchical Data Format (HDF) file and the vbf file is erased. HDF files occupy around 400 MB and are called upon for analysis.

The analysis consists of obtaining a channel's variances from the HDF file, applying the median cut, a profile with a bin size of 10, detrending, and running the clean variance light curves through the 'transient trigger' described above, hereby named the primary trigger. The bin size of 10 is chosen over smaller sizes as it produces significantly reduced baseline fluctuations (compare in Fig 3–7 the rms with bin size 2 or 5 to that of bin size 10) due to their inverse square root relationship. We also obtain a sub-second time resolution of 0.15 s (assuming average L3 rates). A trace of a light curve containing a transient is shown in Fig 3–11 at various stages of the analysis. The trace shown with median cuts and profiling applied (bottom graph) has a clear transient signal with minimal noise compared to the raw trace (top graph) and the trace after median cuts only (middle graph).

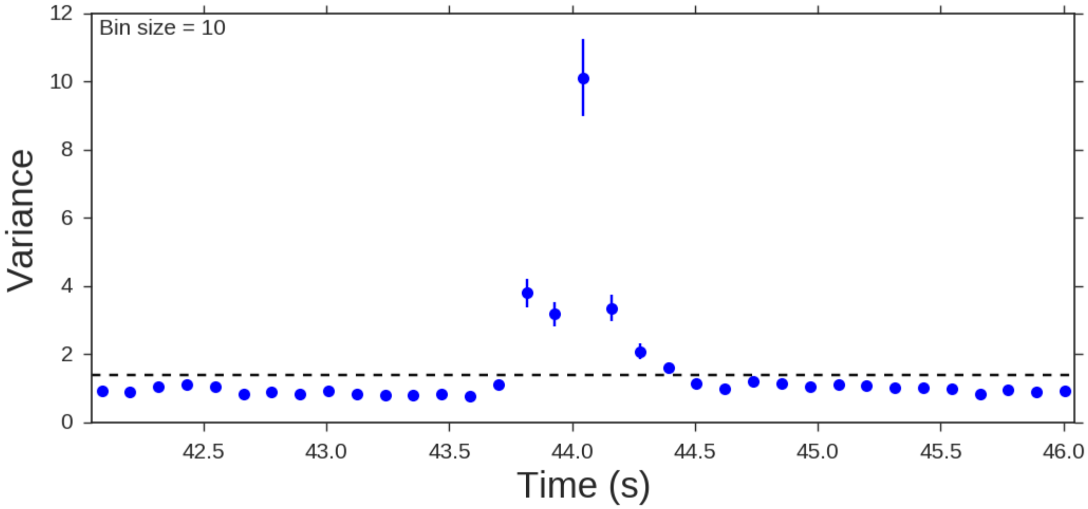

Figure 3–10: Example of a transient signal that the algorithm will detect during the primary analysis. The dashed line is the 3σ above baseline threshold. The bins in this graph are assigned an approximate time based on their bin number and the average L3 rate.

3.7 Secondary Analysis

Runs that registered various triggers across multiple channels were taken to a follow-up analysis. The second analysis done to the variances applies the same cuts and a profile with the same bin width as the primary analysis but uses a different trigger. The secondary trigger is set off when a light curve has at least one bin with value above 5σ and records the timestamp of the highest-valued bin above threshold. The purpose of this trigger is to look for shorter pulses occurring in the pixels in order to image the track of a transient moving through the camera. Instead of calculating an approximate timestamp with the average L3 rate, every bin is assigned a ‘real’ timestamp by taking the average of the timestamps of every variance in that bin (recall that each of these individual variances corresponds to an event set by the L3 trigger and the time of each event is stored alongside the traces).

We plot the light curves of two different channels in the same run as variance over time using real timing (Fig 3–12). As shown in the top graph channel 28 passed the primary trigger while channel 198 was only registered by the second trigger. Note that the spacing between bins (and the time resolution) varies as the L3 rate is not constant. Fig 3–13 shows two camera maps highlighting the pixels that set the primary trigger and those that set the secondary trigger. Color bars are used in both maps to show the relative timing of every triggered channel, this is measured with the approximate timings in the first map but the second map uses real event timestamps. The secondary analysis offers a better approximation of the relative timing between all the triggers as well as a more complete track.

3.8 Stars

During the night many stars fall in the FOV of the telescopes, Fig 3–14 shows the image on a VERITAS sky camera during a typical run. It points to the same location as the telescope cameras where many stars fall within the circle of the camera plane. Due to the telescopes' Alt-Az tracking technique and their large FOV, the cameras rotate around their central pixel so the pixels will rotate through stars.

Bright stars will sequentially register a current in various pixels. A few of the stars shown in Fig 3–14 appear in the on-line current monitor display. In Fig 3–15 we see how various stars inhabit the FOV of the telescopes' cameras and the arc that they trace as the camera rotates. Stars farther from the center will trace a longer arc over the course of the run.

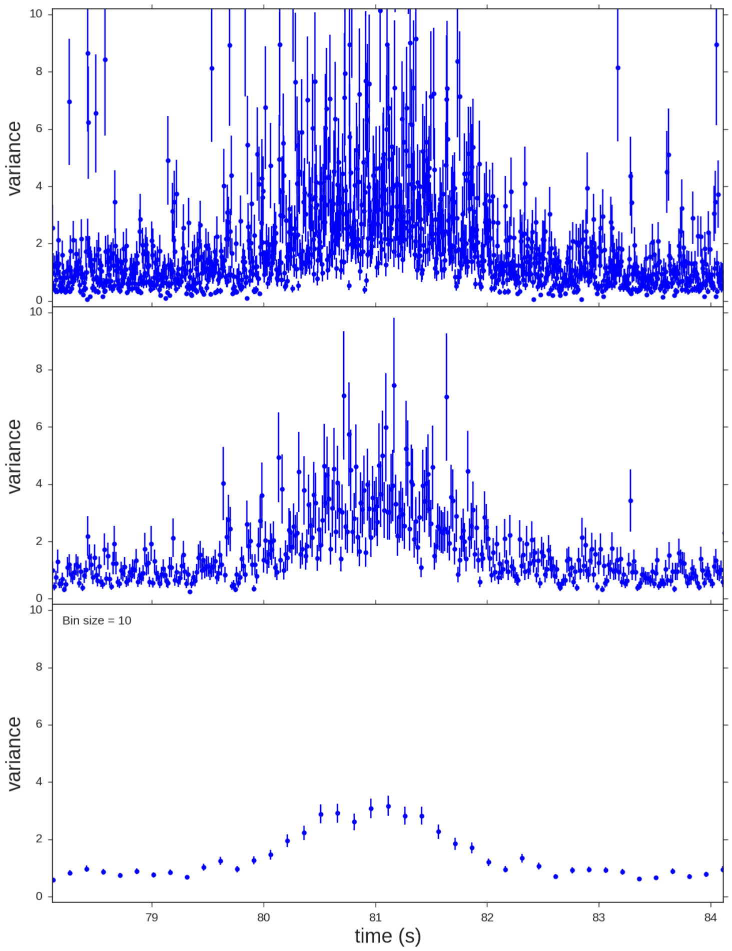

Figure 3–11: A light curve containing a transient pulse is shown at different steps of the analysis. Top: light curve from every variance in a channel. Middle: light curve after the median cut. Bottom: light curve after a median cut and a profile. The morphology of the pulse is present in all cases but the final light curve offers a clean signal with minimal noise.

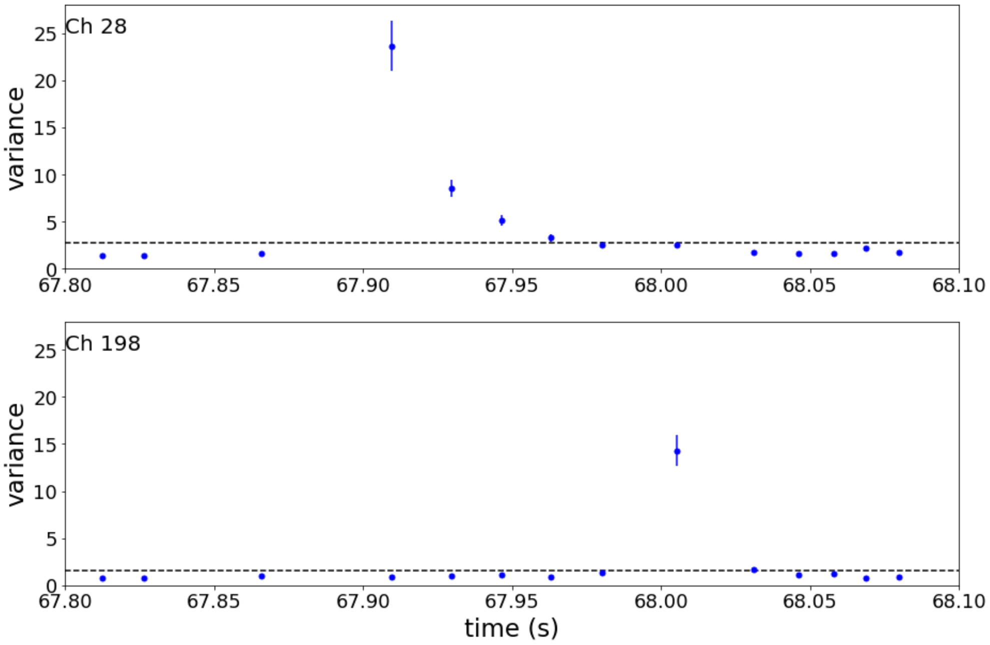

Figure 3–12: Variance vs time for two channels taken from the run shown in Fig 3–13. The bin width is 10 as is standard for the analysis. The dashed line marks a 3σ value above the baseline. Top: light curve from channel 28 that set off the first trigger. Bottom: light curve for channel 198 that only set the second trigger, having only a single data points above 5σ but no neighbors above 3σ.

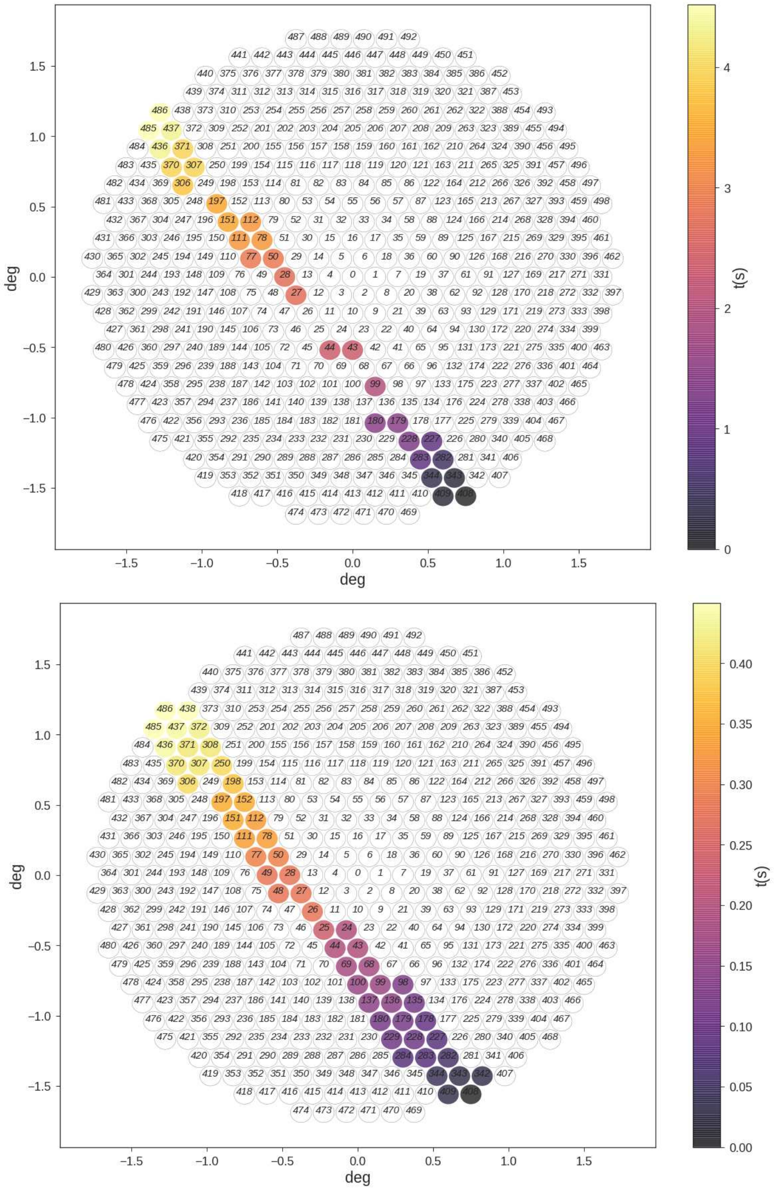

Figure 3–13: Top: camera map with pixels that set the first trigger highlighted with the relative trigger timing approximated using the average L3 rate. Bottom: channels that set the second trigger during the follow-up analysis. Here the trigger time is calculated by taking the average timestamp of all the variances comprising the triggered bin. The read-out rate was higher than average at the time of this signal hence the timespan between transient triggers is shorter than the approximation.

Stars can be seen in the light curves provided they are sufficiently bright. Channels with starlight can cause false alarms in a transient search but they can be used for calibration. Obtaining the peak variance caused by starlight can be quantified directly into a light measure if one knows the magnitude of the star. Determining what range of stellar magnitudes can be seen in the variances can be used to set constraints on the intensity of transient signals that can be detected.

3.8.1 Stars in a pixel

The photocurrent produced from starlight typically does not interfere with data collection unless a star is bright enough that it induces a large current ($> 30\ \mu$A) in a PMT and triggers a shut-down of the high-voltage (HV) supply for that pixel. There are stars such as Zeta Tau ($M_B = 2.7$) that are bright enough to shut off multiple pixels but these are uncommon. A star is represented in a light curve by a slow rise and fall in variance.

Stars in the light curves are distinguished from transients as the peaks appear in an arc of pixels as the FOV rotates. In Fig 3–16 we see the light curves of different channels receiving starlight. The path of the star is evident by the time difference in the peaks of every channel.

During analysis we use the SIMBAD database to find the stars in the FOV [41]. The VERITAS database is queried for the pointing of the telescopes which is used to determine the sky coordinates of every pixel throughout the run. The star's coordinates are cross-referenced with the pixel coordinates to determine which pixels have stars fall in their FOV during the run. Pixels that receive starlight from bright stars are not used for transient analysis. By selecting out pixels with starlight

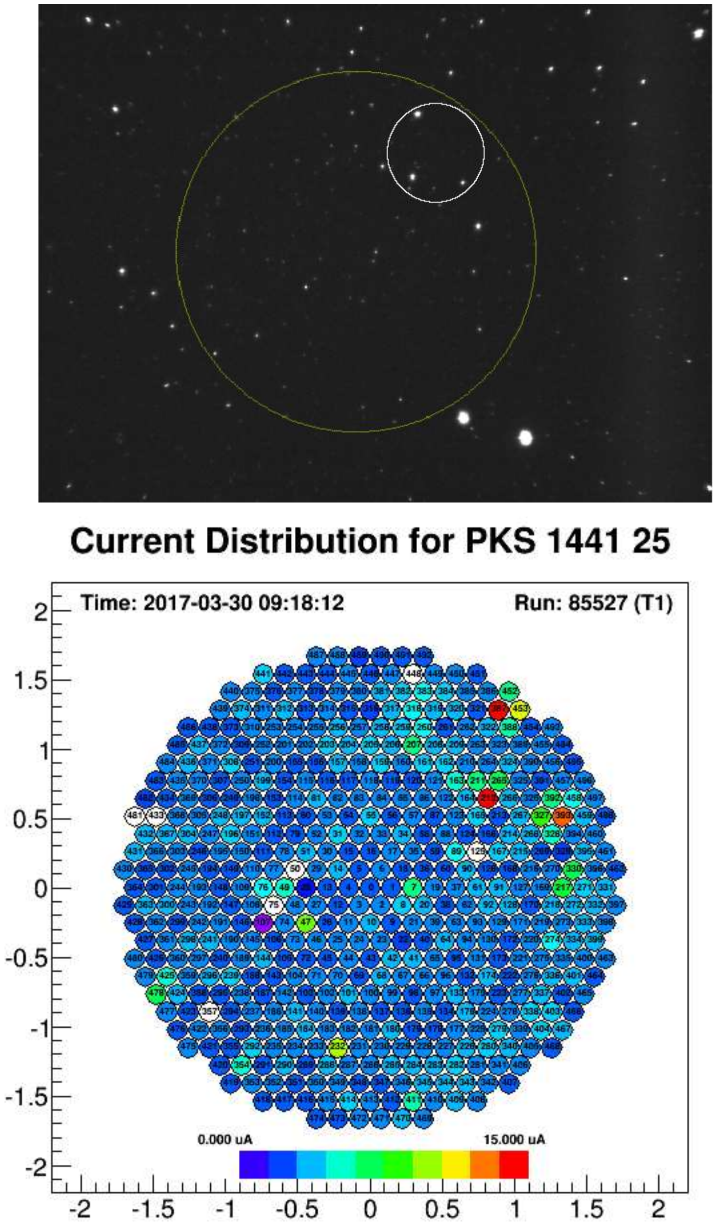

Figure 3–14: Top: View from the sky camera set on Telescope 1 during an observing run. The large circle shows the PMT camera's FOV. Bottom: image of the current distribution in the Telescope 1 (T!) camera during the same run. Note how the location of the pixels with high current in the upper right (red points) match the location of the stars shown inside the white circle.

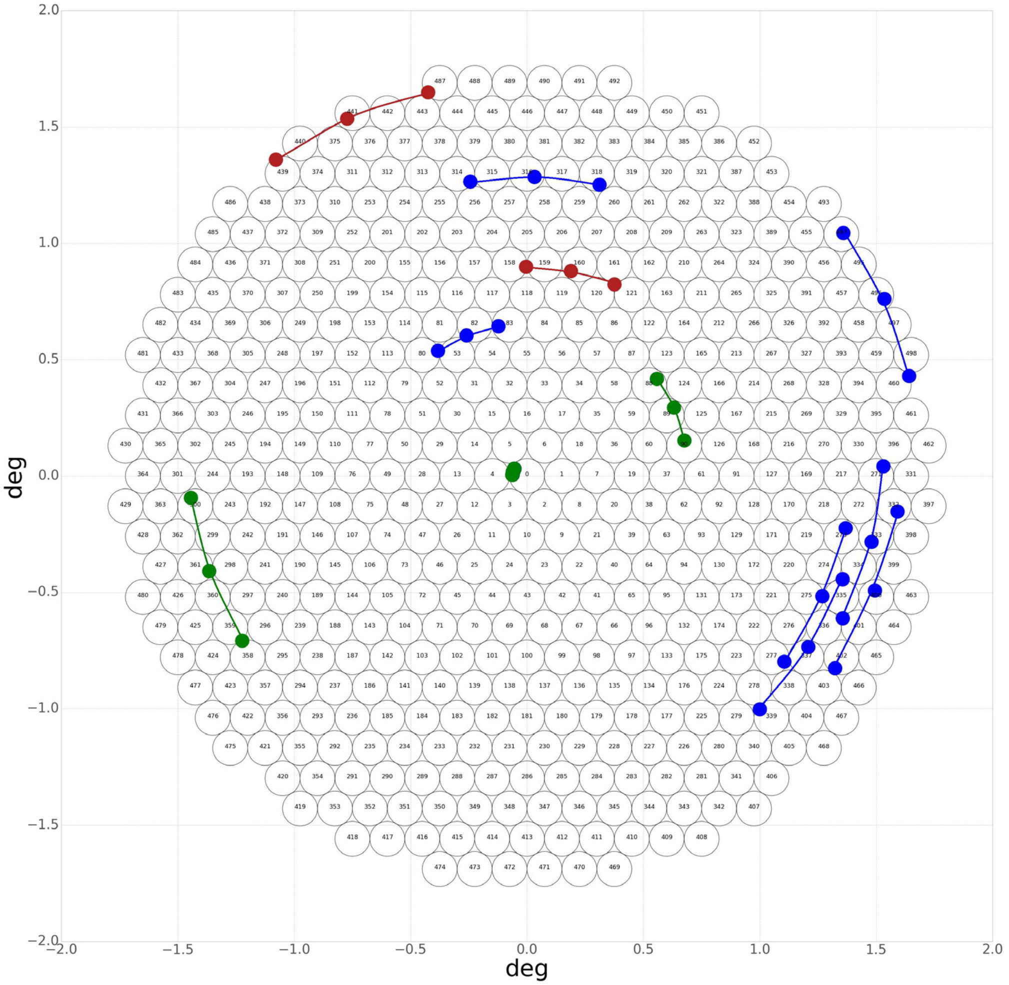

Figure 3–15: Top: Plot of the VERITAS camera plane showing the stars that cross the pixels during a single run. The stars shown range from m$_B$ = 8 (blue circles) to m$_B$ = 3 (red circles). Each star appearing is plotted at three different times: the beginning, middle and end of the run which spans 20 minutes. Lines are drawn to show the arc that each star takes.

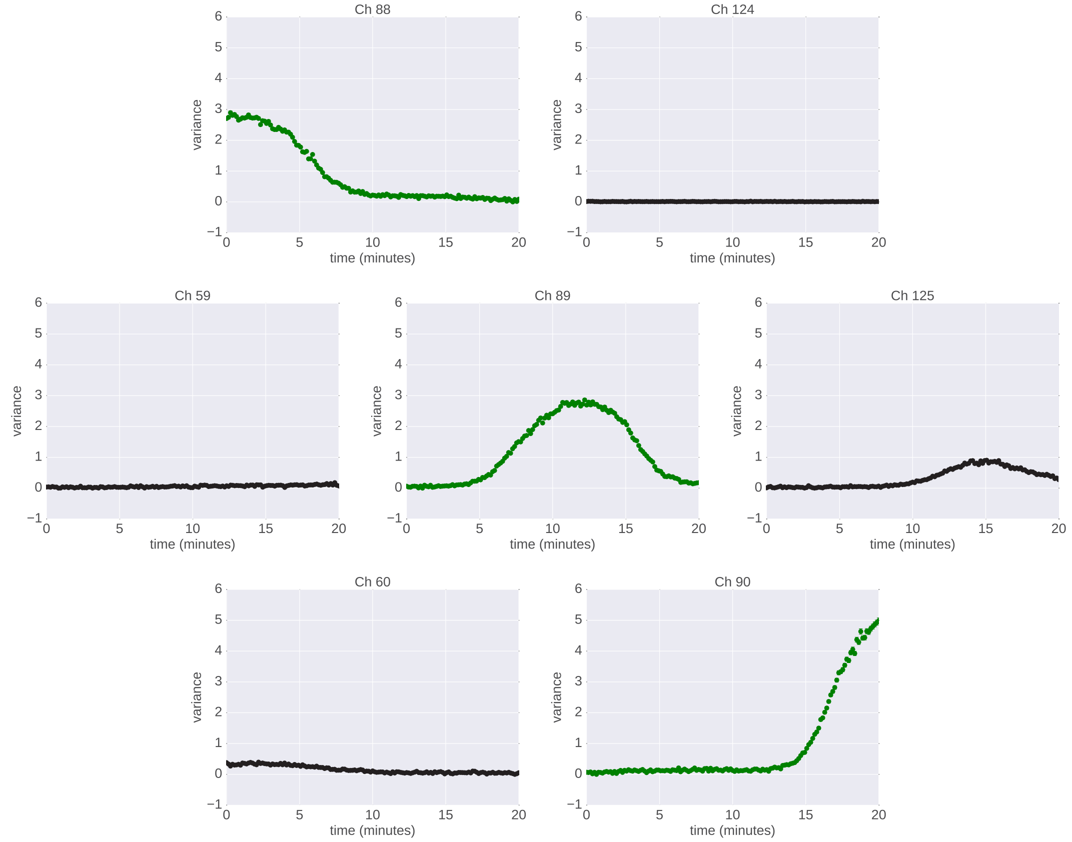

Figure 3–16: The light curves of various channels, using bin widths of 500, are shown in an arrangement analogous to how the PMTs are positioned in the camera. A magnitude 6 star can be seen shining onto channels 89 through 90 as well as 125. The same star and arc is shown in Fig 3–15.

Table 3–1: Filters used in the UBV photometric system including their bandwidth and peak transparency wavelengths.

Filter Type	Approximate $\Delta\lambda$ (nm)	Approximate Peak λ (nm)
U (Ultraviolet)	66	365
B (Blue)	94	445
V (Visual)	88	550

we avoid any false alarms when scanning a light curve for transients. The cost is throwing out pixels that could host both starlight and a transient event but for a simple search through years of data this is only a small loss.

3.8.2 Using Stars For Calibrations

Given that variance is related to the light reaching a pixel, the rise in variance due to a star is proportional to its brightness. The response of a pixel to a particular star depends on the PMT's sensitivity to its emission spectrum. We quantify the spectrum of a star using the UBV photometric system. The system classifies the brightness of a star when seen through one of three wide-band filters that are sensitive to different wavelengths in the domain of near ultraviolet to visible light. The filter types, range and peak sensitivity are described in Table 3–1 and shown as spectra in Fig 3–17. The QE of the PMTs is shown as well: it has the largest amount of overlap with the B-band filter. We compare the peak variance of a star to its blue band, or B-band, apparent magnitude m_B which is the flux of the star as measured through a B-band filter.

The data used to map variance to magnitude consists of 1500 runs from October 2007 to June 2012. SIMBAD is used to find stars that fall close to the center of any channel. An algorithm checks that once a potential candidate is found there are no

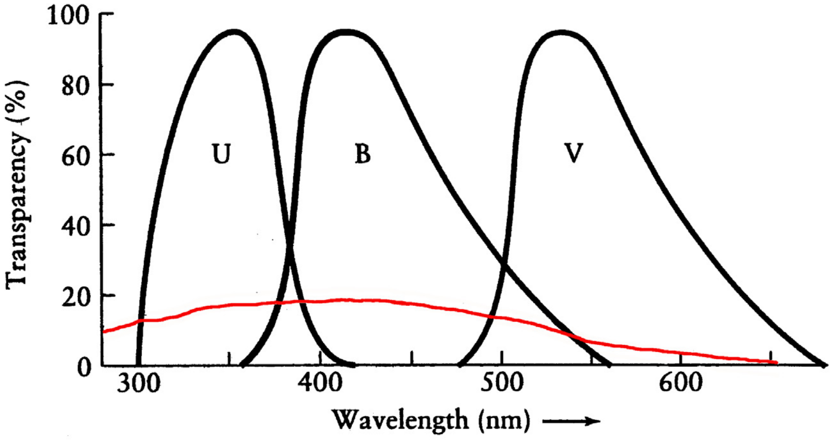

Figure 3–17: Relative transparency of band filters used in the UBV photometric classification system. The QE of a Photonis PMT is drawn in red. The QE rises over the regions covered by the U and B-band filters, indicating that the PMT is specially sensitive to stars with color on those bandwitdths. Image source: adapted from the Institute of Astronomy and National Astronomical Observatory's website [42].

neighboring stars close enough to illuminate the same pixel. These two conditions restrict the number of stars that can be chosen for calibration as it is unlikely that a star will fall close enough to the center of a pixel so that no other pixels are illuminated during its peak. The solution is using hundreds of different runs per season to increase the chances of finding a good star.

Stars form Gaussian shapes in the variances so the peak variance is determined by fitting a Gaussian function and determining its amplitude. A few fits are shown in Fig 3–18 for channels that had stars move through them. Once an isolated star has been found in a channel a Gaussian is fit to the variances. The amplitude of the Gaussian is correlated with the brightness of the star. The width of the Gaussian is inversely correlated with the radial position of the pixel in the camera as it will rotate through a star faster the farther its position is from the camera center.

Performing a search for stars to use for calibration yielded the calibration curves shown in Fig 3–19. The entries have been divided into seasons because a flat fielding[1] procedure is performed inbetween. The gain of the PMTs as well as the variances change every season due to flat fielding. There are a few reasons to explain the scatter in the calibration curves: attenuation of starlight and different star colors. Starlight is attenuated in the atmosphere and the amount of attenuation depends on atmospheric conditions that vary over time as well as the incidence angle.

---

[1] flat fielding is a calibration technique where the HV of the pixels is adjusted so that their gain is uniform throughout the camera

The variances from stars with similar B-band magnitudes can vary if their spectra have components outside the B-band. Fig 3–17 shows that the QE of a PMT overlaps with both U and B-band filters. If two stars have the same m_B but different U-band magnitudes then the deviation in the light curve will be larger for the one with lower m_U. The effect from light in the U-band contributing to the scatter in the calibration curve can be reduced by measuring the magnitudes of both bands or setting a threshold on m_U. These corrections are beyond the scope of this thesis.

3.8.3 Limiting Magnitude

The calibration curves can be used to find the apparent magnitude of the dimmest light source that can be detected by our analysis. The limiting magnitude is defined as the 3σ value of a light curve, which is the same threshold as the primary trigger for transient detection, which varies according to the bin width. Using the relationship between variance and magnitude (Fig 3–19) and that of variance and bin width (Fig 3–7) we can fit a linear relationship between the limiting magnitude and a particular bin width.

In Fig 3–20 we show a calibration done for the central pixel during a run taken in January 2012. The standard deviations are calculated from the channel's light curve and then converted to m_B using the 2011/2012 calibration curve. 5σ values are shown as well as it is the threshold for the secondary trigger. In our archival search we utilize bins of 10 variances each thus achieving a limiting magnitude of $\mathrm{m}_B = 8.9$. As the number of variances per bin is increased the amount of statistical fluctuation is reduced so we achieve better sensitivity to dimmer events.

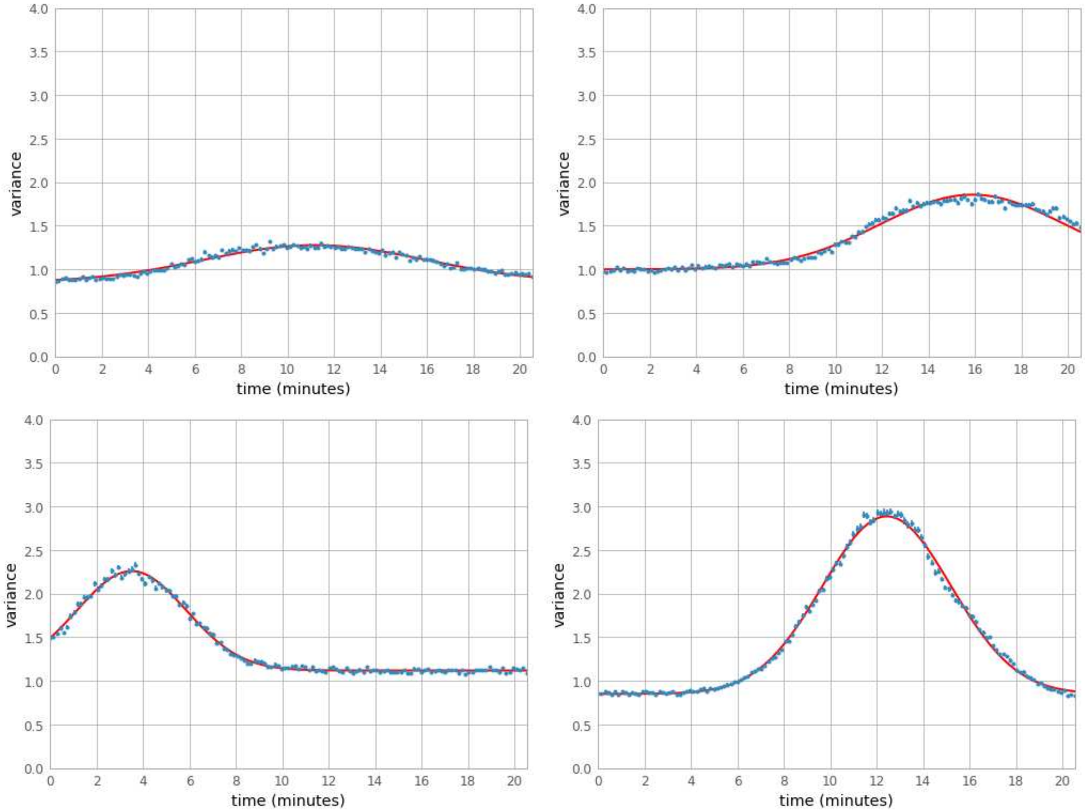

Figure 3–18: Variance vs time with Gaussian fits applied. Each channel is occupied by a star of m$_B$ (clockwise from top left) 9.23, 8.3, 7.03 and 6.5. Note that the bin size is 500 and the pulses have different widths, meaning that the time it took a pixel to cross a star was different in each case. Pixels farther from the center of the camera rotate through a star faster than those closer to the centre. The width of the Gaussian decreases with the pixel's distance from center since a star spends less time in the pixel's FOV.

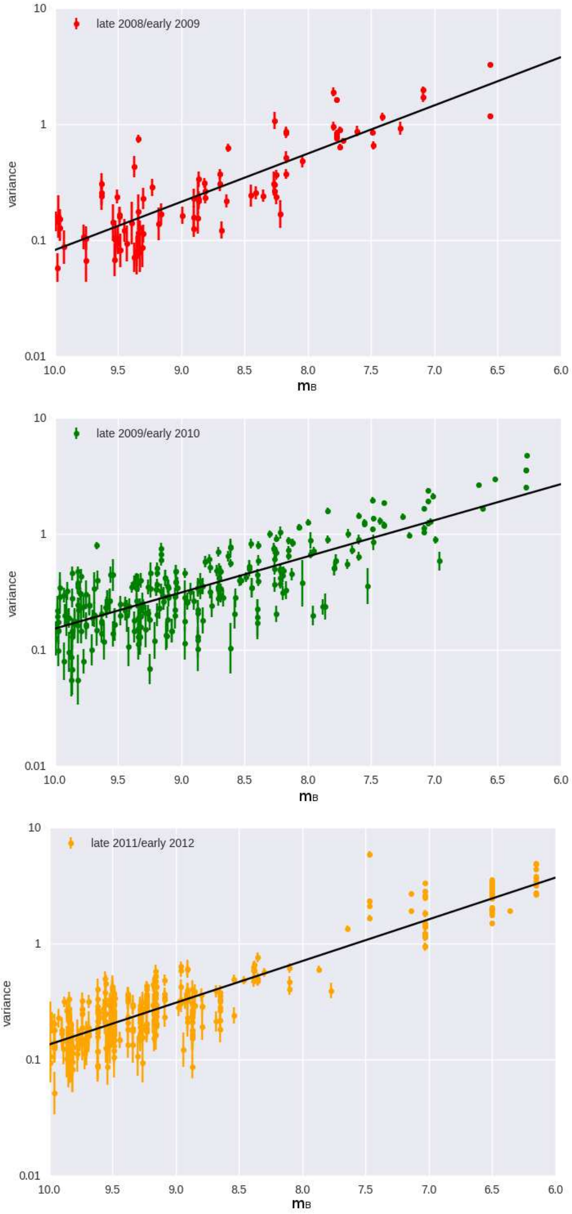

Figure 3–19: Calibration curve using stars found in the 2008/2009, 2009/2010 and 2011/2012 seasons. The curve for the 2007/2008 and 2010/2011 is not included as only a small sample of calibration stars were found. The curves show a correlation between a channel's maximum variance and the apparent B-band magnitude of the passing star. A fit is drawn in each graph as a black line.

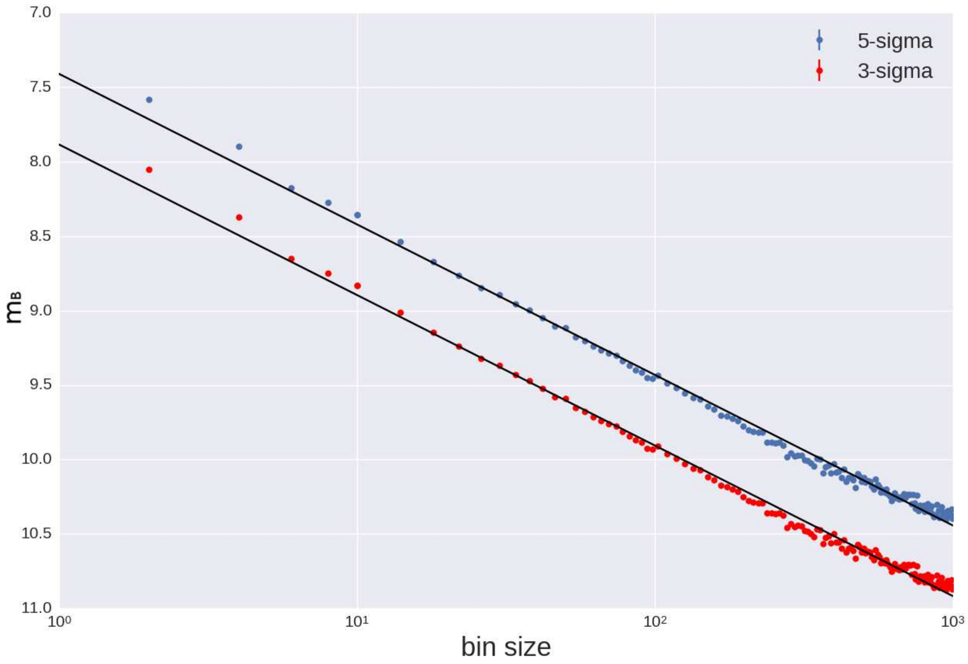

Figure 3–20: Sensitivity curve showing how the limiting sensitivity of a transient search, in terms of m_B, varies depending on the size of the variance bins. The plot is produced by calculating 3 and 5 σ values of the light curve and converting them to apparent magnitude using one the calibration curves in Fig 3–19. A linear fit is drawn across each set of data points.

3.8.4 Limits on Transient Detection

The type of transients that can be detected successfully by the primary analysis is determined by its limiting sensitivity and time resolution. A transient will not be detected if its duration is smaller than the time resolution (0.15 s), or its brightness is below the limiting magnitude ($m_B = 8.9$), or both. Millisecond transients such as optical flares from a LMXB will not be detected; the fastest transient that the algorithm will detect is a meteor. Stellar occultations are good candidates for detection as the timescale of an occultation is longer than 0,15 s, even when the object eclipsing a star is sub-kilometric.

There are upper limits to transient detection as well: a run has a 20 minute exposure time so slow-fading transients, such as a GRB afterglow, can not be contained in a single set of light curves. The slowest transient that can be contained in a single run is a flare from a red dwarf if the dwarf's quiescent B-band brightness is below 10 so that it is kept in the analysis. Transients brighter than Zeta Tau, such as novae and supernovae, will disable the HV in the pixels and therefore remain unseen by the analysis. Meteors and satellite flares can vary in their brightness, thus some can be detected by the PMTs without shutting off the current. In summary, terrestrial transients fall well within the limits of the analysis and can be detected. The majority of the astronomical and astrophysical transients discussed in chapter 1 fall outside our limits.

3.9 Pathologies

NSB fluctuations include a wide array of pathologies that can not be removed from a channel's variances with the methods discussed above. A blind search for short transients based on variance will cause false alarms by triggering on variances caused by pathologies. These pathologies include a strong rise in photocurrent due to lightning or a vehicle passing by. Unfavorable weather conditions can affect the variance as well; clouds can reflect light away or into the cameras. Fig 3–21 shows two variances from different nights affected by strong weather. The number of channels in a run affected by weather is minimized by choosing to only analyze runs ranked as a ‘A’ weather, meaning that there were no clouds in the FOV.

PMTs Without Current

The HV of a PMT is turned off during the run if current values exceed 30 μA for four seconds. While the HV is off the current sensors will simply read out that there is zero current, and variances during this time period will form a flat line. A light curve where the HV was turned off for 8 minutes is shown in Fig 3–22.

Light curves corresponding to pixels whose HV was turned off at some point during the run are removed from the analysis to avoid false alarms. To determine which pixels were shut down during a run the database is queried for current samples using MySQL. MySQL is a database management system based on ‘Structured Query Language’ (SQL), a standard language for communicating with databases. Channels with at least one sample valued at zero are discarded from the analysis.

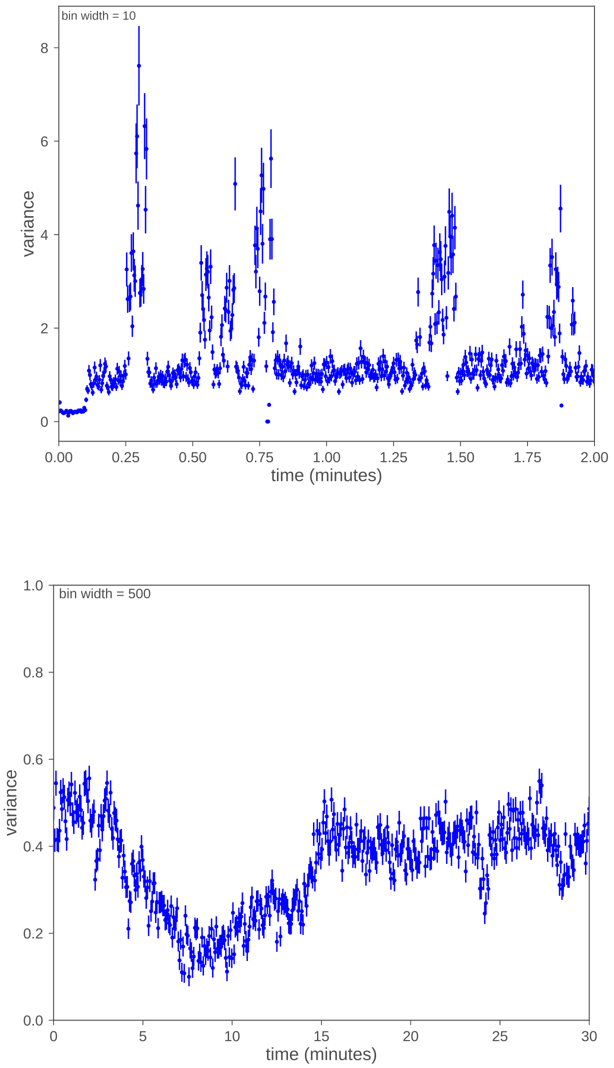

Figure 3–21: Variances affected by weather. The top graph shows the variance during a thunderstorm. The occasional spikes in variance are not from lightning but rather from the HV being turned off by lightning and then returning to power. The bottom graph shows a variance during a cloudy night. The baseline fluctuates throughout the entire run because ambient light is scattered by the clouds.

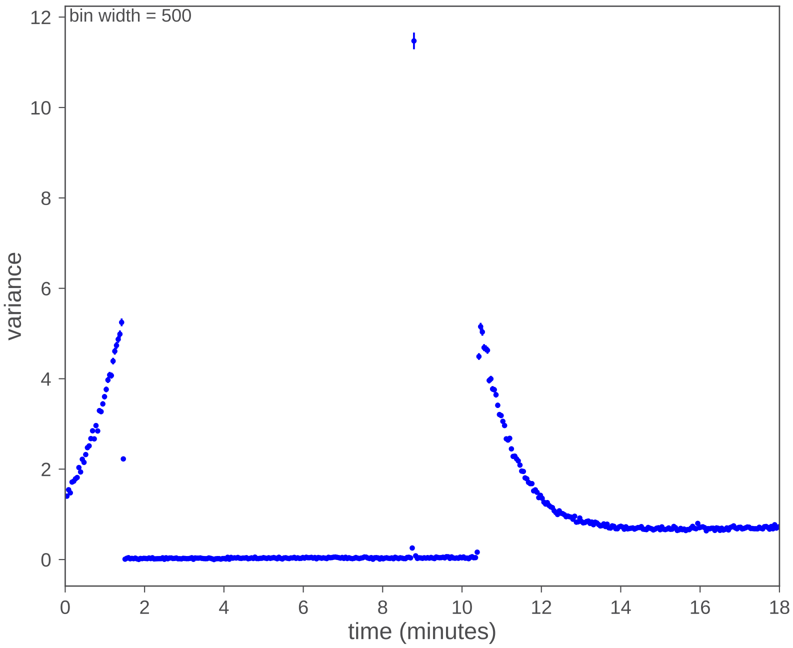

Figure 3–22: Variance affected by a bright star crossing the FOV. The rise in photocurrent causes the HV to be turned off in that channel until the pixel rotates past the star. The spontaneous rise in variance near the 9 minute mark is caused by the HV turning back on automatically to check if current levels have dropped below threshold.

CHAPTER 4
Results

4.1 Archive Search Summary

We have performed a search through 4066 runs using the techniques described in chapter 3. The runs were selected from the V5 era with the criteria that they had a full 20 minute exposure and were assigned grade ‘A’ weather. The primary analysis with a trigger threshold of three consecutive bins above 3σ was performed using Telescope 1 and 2 data only while the secondary analysis (trigger on a single bin above 5σ) used all four telescopes. The reason for using two telescopes first is that the goal of the first analysis was to check if interesting signals could be found in some of the telescopes. While analyzing T1 data first could have been enough information to determine whether or not to proceed to the secondary analysis, by using T1 and T2 in conjunction we obtained better assurance that a multi-telescope signal was detected.

During the primary analysis no point-like transients were found appearing in the same pixel in both telescopes. There were 117 instances of runs that set multiple triggers and thus became candidates for the secondary analysis. 30 of these candidates were false alarms in which the triggers had no coincidence in timing or location in the camera. The remaining 87 instances have been labeled as ‘transient events.’

4.2 Secondary Analysis Results

The unifying characteristic of all transient events is that neighboring pixels were illuminated in sequence. The variances of their corresponding FADC channels would show a time difference between peaks no larger than a few seconds. Fig 4–1 is an example of a peak in the variance that 'moves' from one channel to another.

Further analysis showed that the location and timing of the triggers corresponded to the light source crossing the field of view (FOV) of all four telescopes and illuminating a track of pixels. The tracks were straight lines, no arc shapes were found. The events are likely terrestrial (recall that celestial bodies like stars appear to move in an arc around the camera center due to the tracking of the telescopes).

Every triggered channel is assigned a trigger time equal to the time stamp of the highest valued data point. The duration of a transient event is measured as the time difference between the channel with the smallest trigger time and the channel with the largest time. As an example, figure 4–2 shows the variances of two channels containing the initial and final signal from a transient, based on this we estimate that the event lasted about 0.2 seconds. It was found that the duration of these events varied from a fraction of a second to a fraction of a minute. The duration of the event is not representative of the lifespan of the light source itself but simply the approximate amount of time that it fell within the FOV.

We present our results using two categories: transients whose observed duration was a fraction of a second and those lasting longer than a second. Four of the seconds-long 'slow' transients had tracks that shifted significantly between the telescopes, signifying that the light source was sufficiently close to the array that each telescope saw the event from a different angle.

4.2.1 Sub-Second Transients

12 sub-second transients have been found. The most distinguishing characteristic is that 5 transients had tracks commencing and ending in the pixels located at the edges of the camera. In Fig 4–3 we show the image of a transient crossing the diameter of the camera in the span of 0.25 s, the highlighted pixels are those with a peak value passing a 4σ threshold, that causes some channels in the path of the transient to not be represented in the graph. Circles are drawn in the channels above threshold, the color gradient corresponds to the timing and the size of the circles represents the relative value of the peak variances. The peaks become progressively smaller as the transient moves through the camera, this indicates that the light source became dimmer.

The angular velocity of a transient is calculated by measuring its change in position on the camera map over time. Fig 4–6 shows the timing and position of the pixels along the track relative to the initial location of the transient on the camera map. By fitting a line to this distribution we calculated an angular velocity of 15.4 ± 0.6 °/s. The other telescopes had similar peaks in the light curves (Fig 4–4) and tracks in the camera plane (Fig 4–5).

The lack of a remarkable parallactic displacement between telescopes indicates that the light source was at least 65 km in distance from the array, otherwise the images would appear shifted from one another. We conclude that this transient

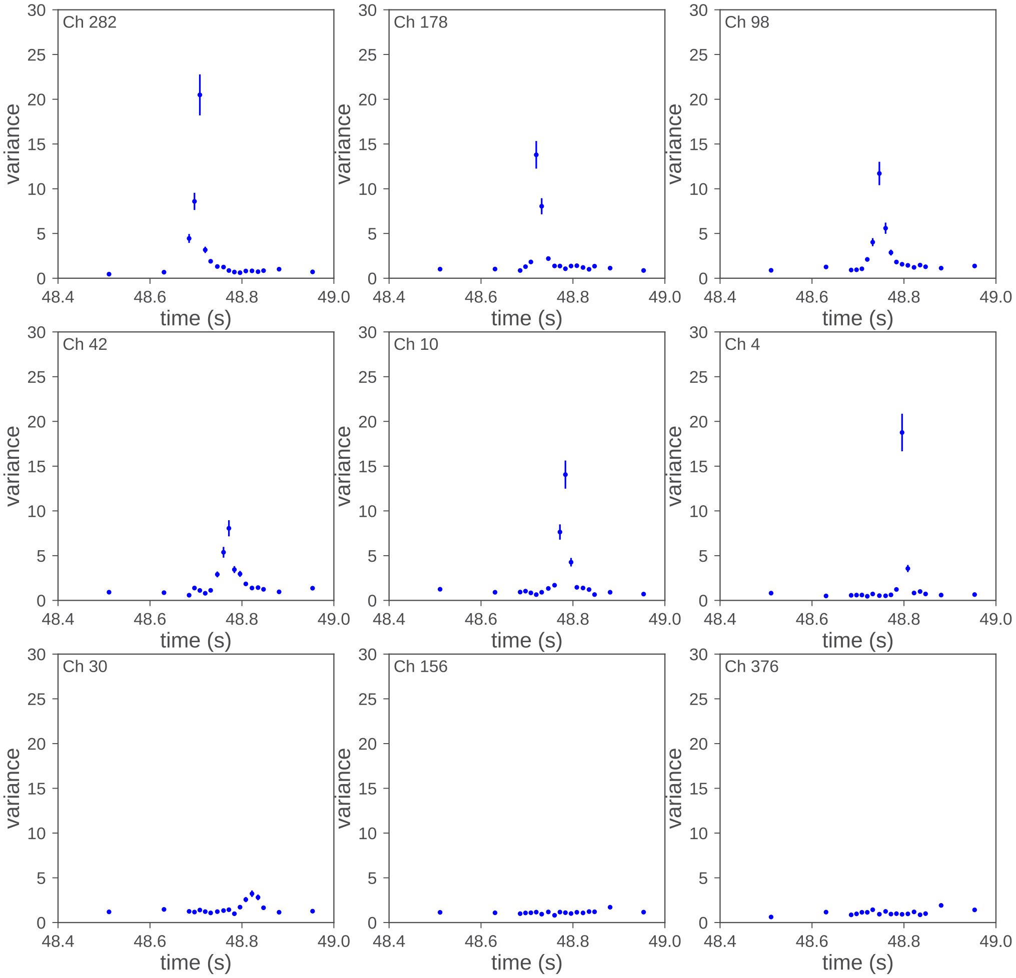

Figure 4–1: Near the 1 minute mark of run 37918, the variance in multiple channels peaked over a tenth of a second. Shown here are a few of the channels with a variance peak. The timing difference between the signals suggests that an object traveled through the FOV of the camera. Note that the spacing of the data points decreases during the transient because the read-out was triggered by the moving light. The channels are shown in the camera map in Fig 4–3.

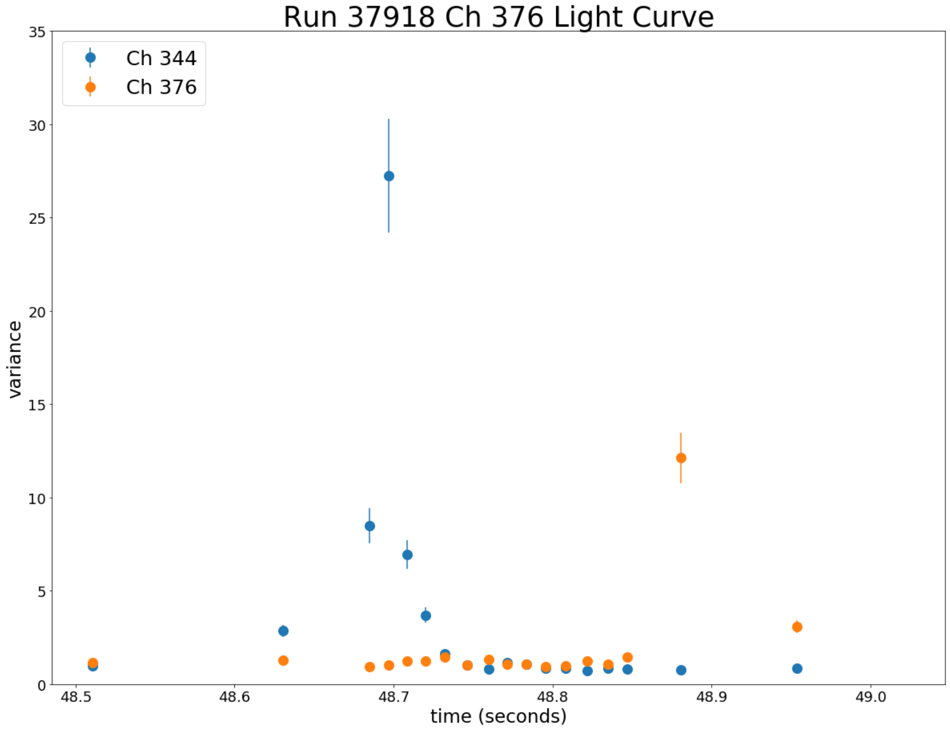

Figure 4–2: Two light curves during a transient event showing peaks a fraction of a second apart. Channel 344 has the earliest trigger time of all the channels in the event while channel 376 has the latest time. The event time, equal to the difference between earliest and latest trigger timings, is about 0.2 seconds.

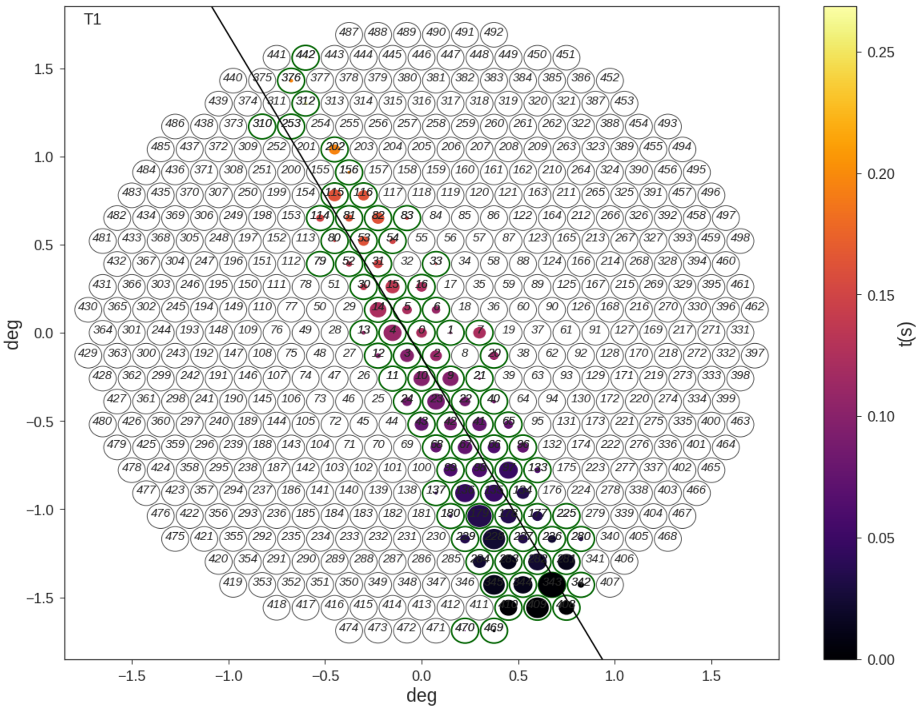

Figure 4–3: Track of pixels on the PMT camera map that were illuminated by a moving light source. The highlighted channels (green outlines) are those with variance values above 4σ. The timing of each channel is that of its highest valued bin and their peak value is represented by the size of the inset circles. A linear fit is drawn to show the approximate position of the light source.

faded over its duration in the FOV, it had a fast angular speed, and lacks measurable parallax, as the displacement is smaller than a pixel. These observations fit the characteristics of a bright meteor evaporating in the atmosphere. A meteor evaporating at an altitude of 100 km with an average angular speed of 15.1 ± 0.6 °/s would have a speed of 27 ± 1 km/s which is normal for a meteor.

Incomplete Transient Events

The 7 transients with an incomplete path appear to begin near the center of the camera and end near the pixels on the edge or vice versa. We show the light

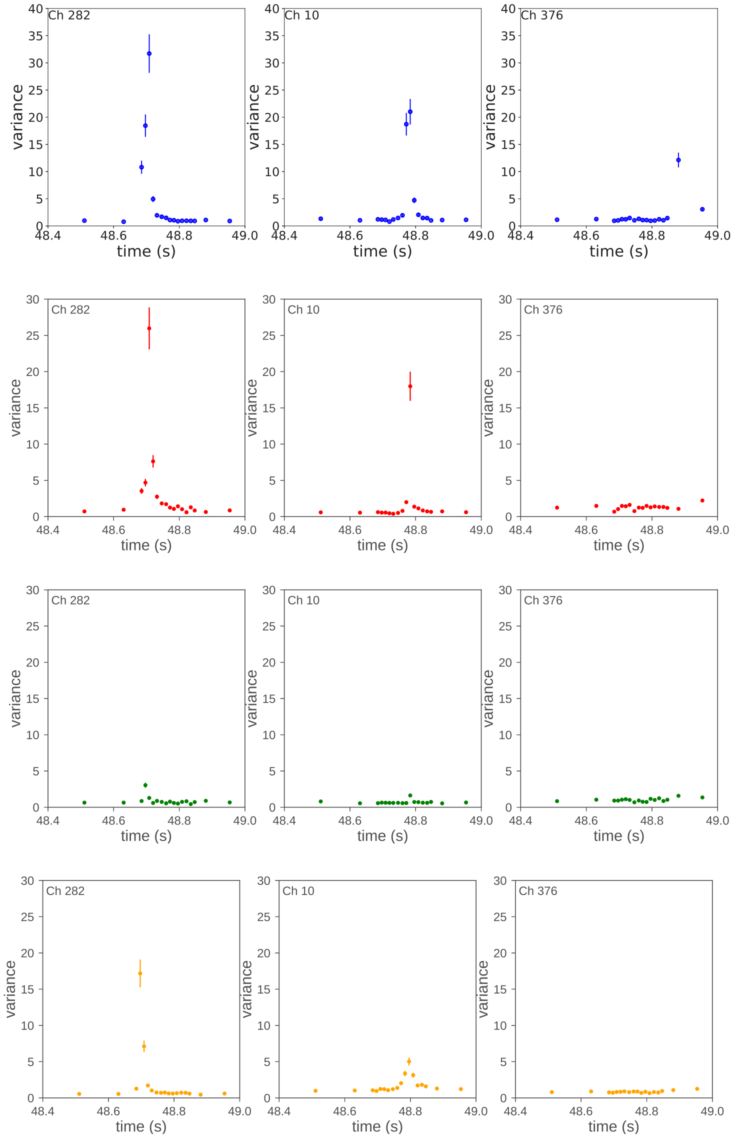

Figure 4–4: Light curves of channels with a signal seen run 37918. The variances of three channels for Telescopes 1 (blue), Telescopes 2 (red), 3 (green) and 4 (yellow) are shown; each light curve has a peak during the beginning, middle or end of the event. The peaks in Telescope 3 have smaller amplitudes than those in the same channels of the other telescopes. The primary reason for this discrepancy is that there's a small amount of parallactic displacement between the light source and the array. The displacement causes the signal to be distributed differently in each telescope across neighboring pixels.

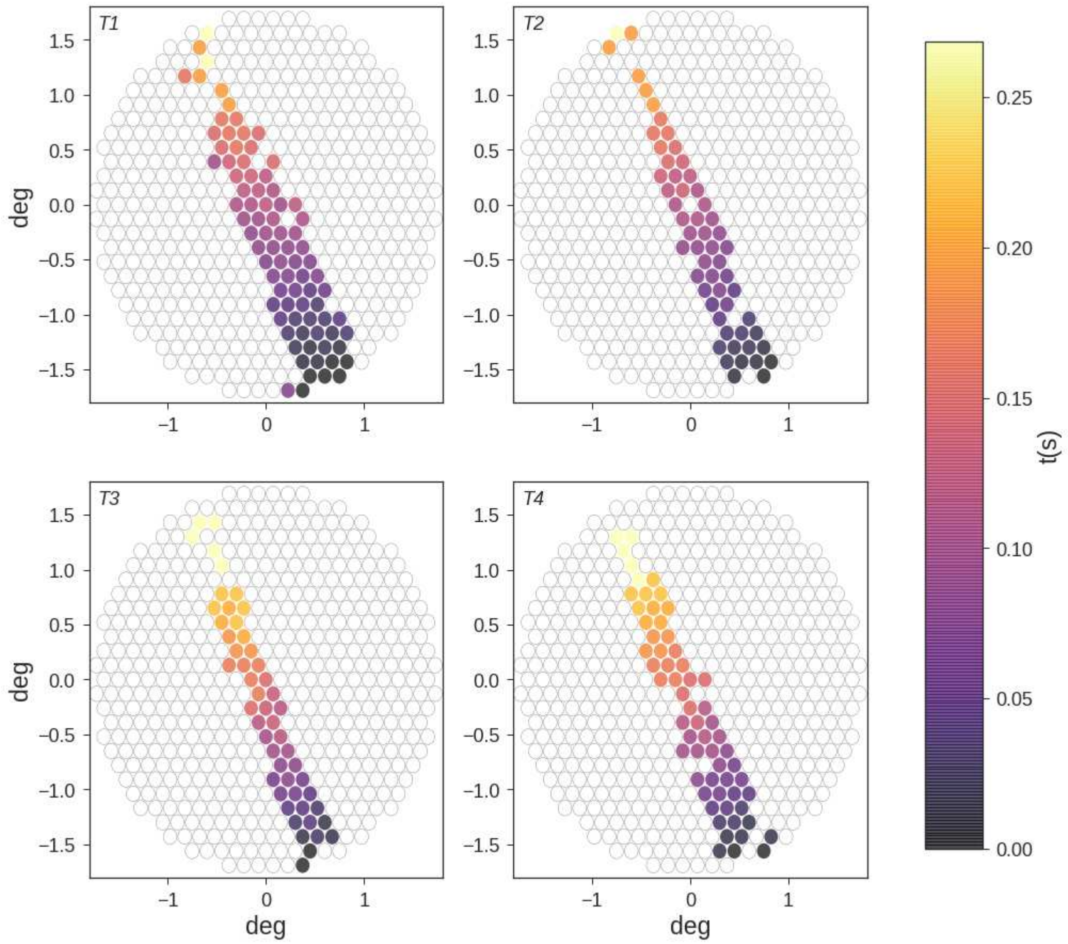

Figure 4–5: Camera map of each telescope during run 37918 showing the illuminated track formed over 0.25 seconds. The tracks do not show a noticeable shift from one another, this suggests that the light source was over 65 km away from the array. There is a gap near the end of every track possibly caused by the light source being a meteor. Meteor light is not consistent as it is produced in spontaneous bursts of ionized air particles.

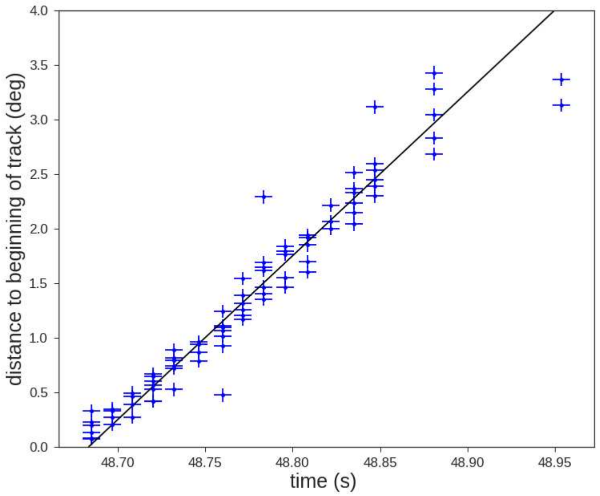

Figure 4–6: A graph of the timing and position of every channel triggered by the transient in run 37918. The position of each channel is calculated as its distance from the beginning of the track. We fit a line to this distribution to determine the angular speed of the transient.

curves of a transient event occurring in run 61283 (Fig 4–7) as well as a map of the tracks (Fig 4–8). The signal starts from the lower left edge of the camera and ends near the center (that is, the variance values of those channels are below threshold). Similar to the event in run 37918 this fading transient shows no significant parallax and a fast angular speed of 6.3 ± 0.5 °/s. Assuming the event was caused by a meteor at altitude of 100 km its speed would be 11 ± 1 km/s. The reason the event 'fades' before crossing the camera might be that the meteor evaporated completely or became too dim.

A notable feature shared by these fast transients is that they successfully triggered the telescope read-out (Fig 4–9). A possible explanation for this is that a bright transient passing through the camera will 'spill' light into multiple pixels. The optical point spread function (PSF) can expand an image into multiple pixels

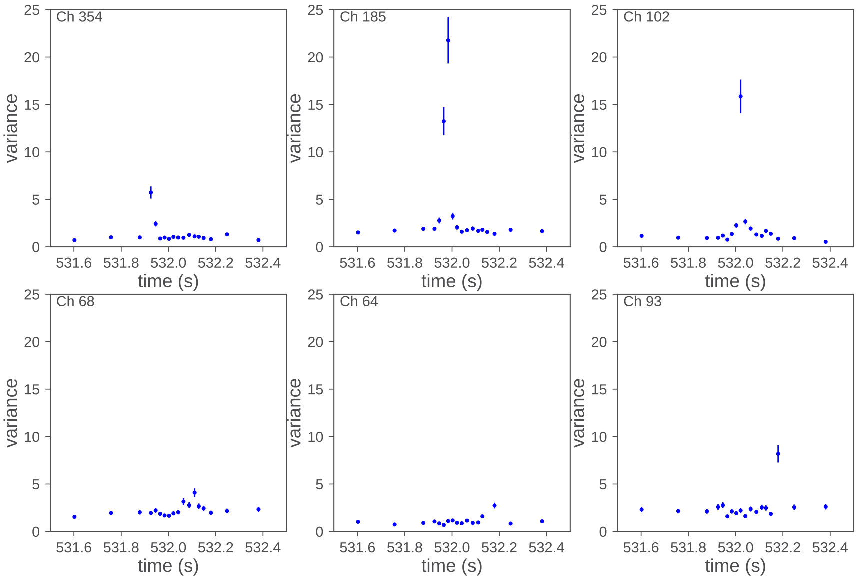

Figure 4–7: Light curves from run 61283 for different channels in Telescope 1. The L3 trigger was fired at a high rate by the transient so the time intervals between variances are smaller, allowing for a finer time resolution.

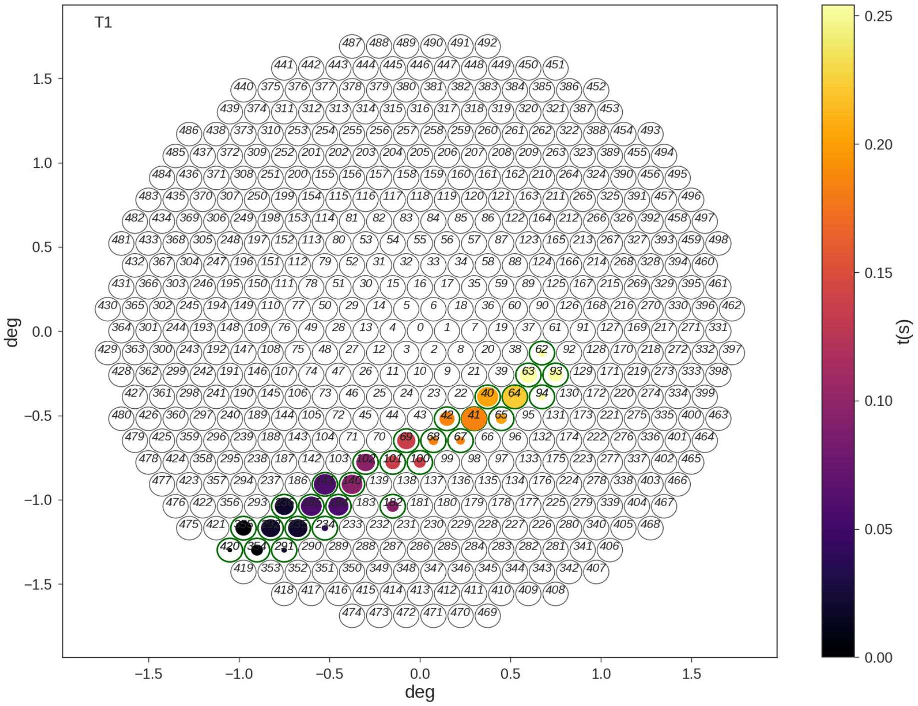

Figure 4–8: The track for the event in run 61283 shows an image beginning at the edge of the camera and vanishing near the middle. Only pixels with a 4σ peak are highlighted with their relative peak values shown by inset circles. The sudden ending of the track might be due to the light source being a meteor that evaporated before crossing the entire FOV.

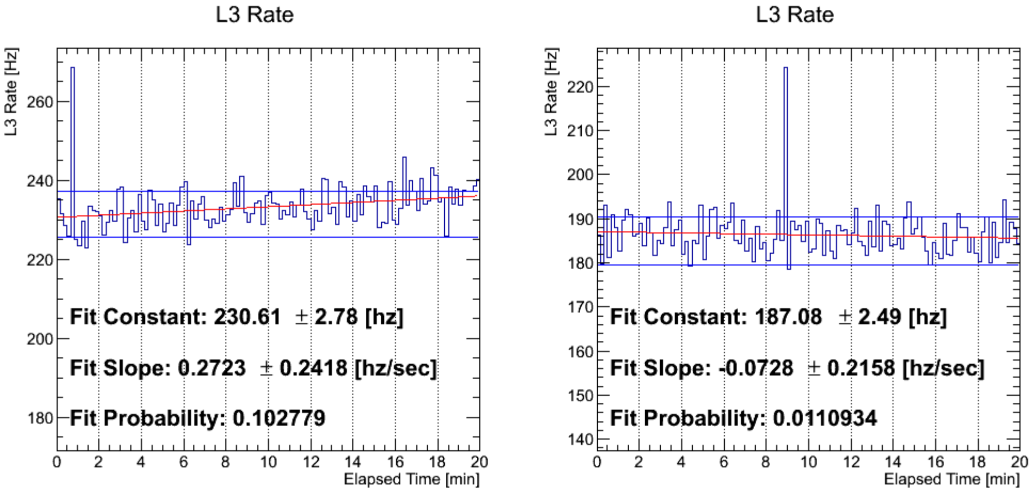

Figure 4–9: The L3 trigger rate for runs 37918 and 61283 which both had a sub-second transient event. A large increase in the read-out rate occurs near the 1 and 8 minute mark respectively, which is near the time where the transient signals were measured. The telescope read-out was likely triggered by the transient illuminating various pixels simultaneously.

which increases the chances of setting the L2 pattern trigger. The time resolution of the light curves is finer for the duration of these transient events thanks to the increased read-out.

4.2.2 Slow Transients

The second type of transient events last longer than a second. 75 of these events were found and all share the trait that their tracks completely cross the camera suggesting that the light source was either reflecting light or producing it artificially so it does not fade over time. 71 of the transients appear in the same location on all four telescopes. We highlight a transient event that occurred during run 59465 as an example: its light curves show a moving light source (Fig 4–10) and a signal crossing the FOV of every telescope over 3.4 s (Fig 4–11). There is no significant increase in the L3 rate during this event.

Events With Parallax

One of the four events with parallax is shown in Fig 4–12. We can use the timing and displacement of the images to calculate their altitude and velocity. A line was fit to each track and then placed on a single plane to compare their position in the cameras (Fig 4–13). The largest displacement occurs between telescopes 1 and 4 whose images are shifted by 8 pixels. Telescopes 2 and 3 had the smallest displacement, no larger than the size of a pixel (0.15° in diameter).

Using the parallactic displacement we calculated that the altitude of the light source was 10 ± 2 km. The angular speed and the velocity is approximately 1.18 ± 0.05 deg/s and 740 ± 30 km/hr. The altitude and velocity are comparable to that of a commercial aircraft.

4.3 Future Work

The events found in the V5 era search corresponded to light signals from terrestrial transients. There were no four-telescope point-like signals found. In this section we discuss how we can proceed with future optical searches.

4.3.1 Archival V6 Data

The photomultiplier tubes were upgraded in 2012, switching from a Photonis model to Hamamatsu. The Hamamatsu PMTs have superior QE. They reach a peak 35% QE for ≈350 nm light compared to the Photonis 20% peak QE (see 4–14). There are now five years of data recorded since the upgrade. Archived V6 are similar in structure to V5 and can be studied with the methodology described in chapter 3.

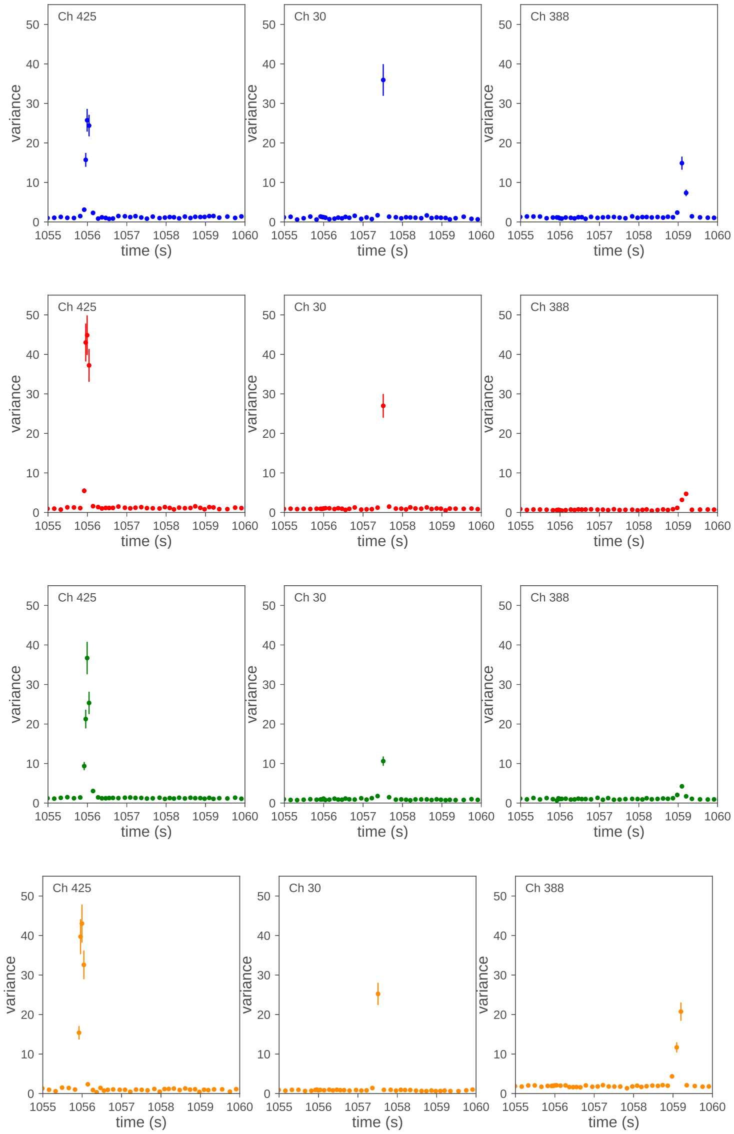

Figure 4–10: Light curves produced for a few channels during a transient event observed over 3.4 s. Each row corresponds to a different telescope starting at the top with Telescope 1. During the event there was no significant increase in the L2 and L3 rates. The signals were recorded serendipitously during triggers set by air showers.

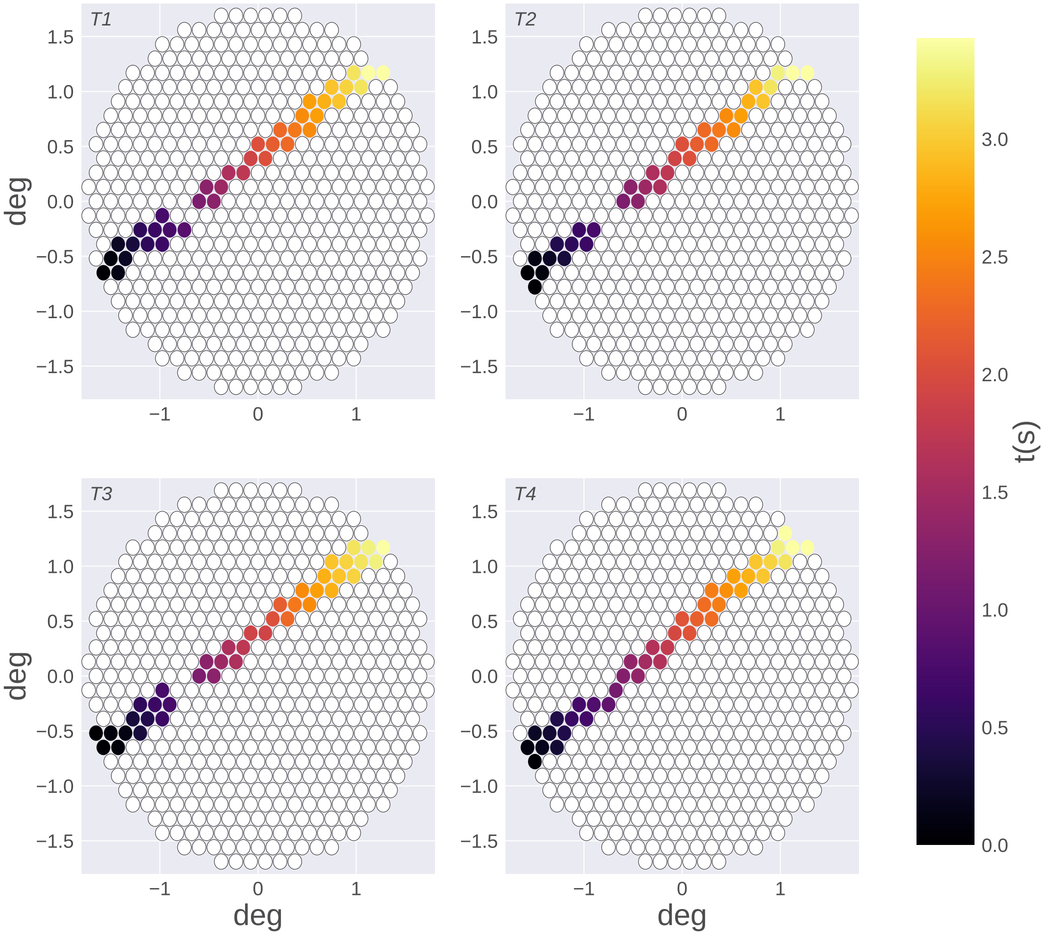

Figure 4–11: Transient event during run 59465 as imaged by each telescope. The tracks do not show significant parallactic displacement

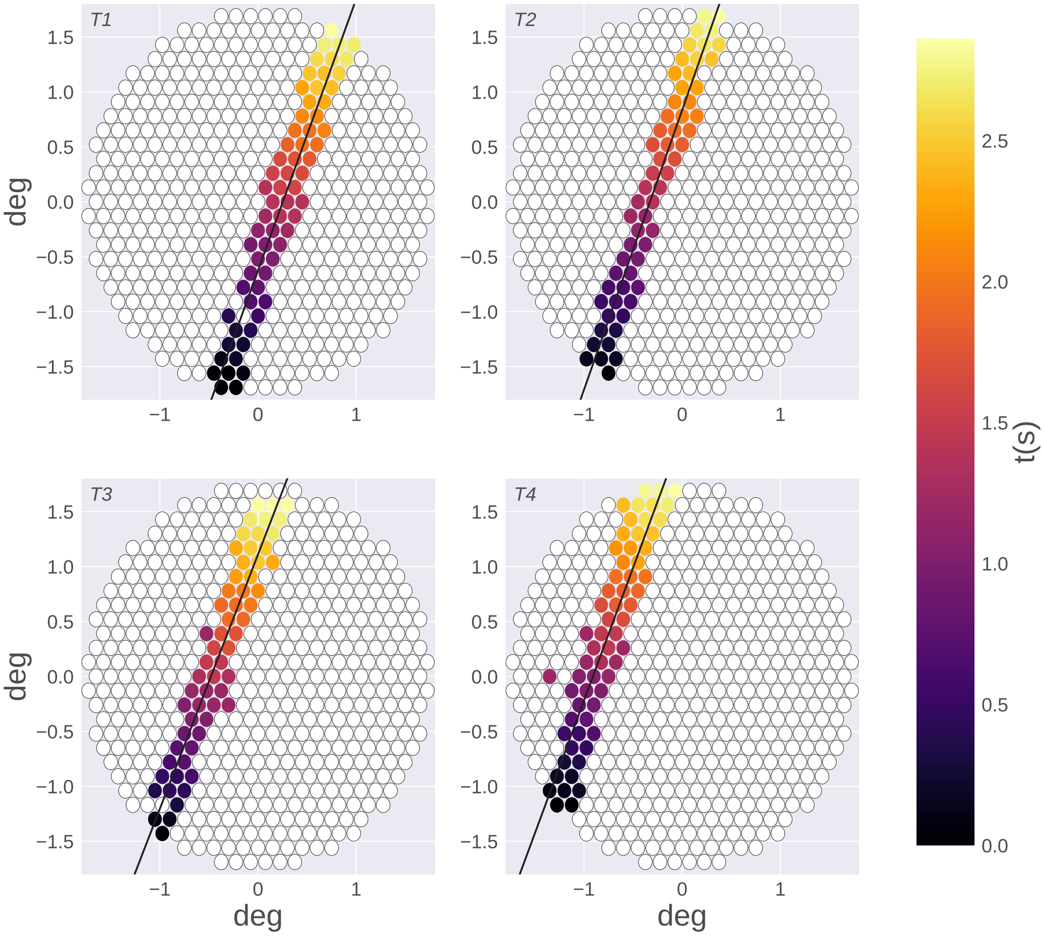

Figure 4–12: Transient event as imaged by each telescope. A line is drawn in each camera to show the approximate position of the light source. The lines are parallel but shifted from one another which indicates a significant angular displacement between the light source and the array.

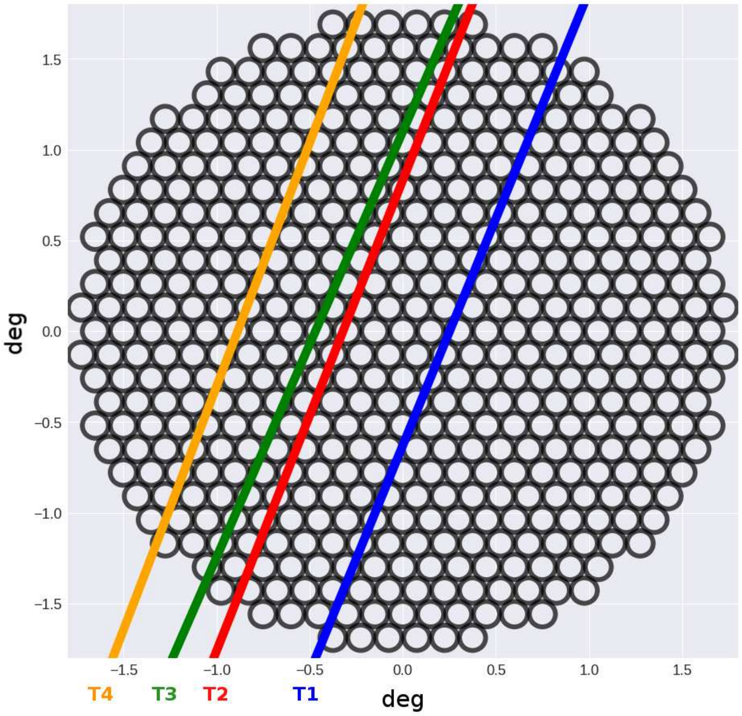

Figure 4–13: Tracks from different telescopes are shown in the same camera plane. Each track shows the location of the image of the same flying object. The parallactic displacement between the tracks implies that the object flew at an altitude of about 10 km.

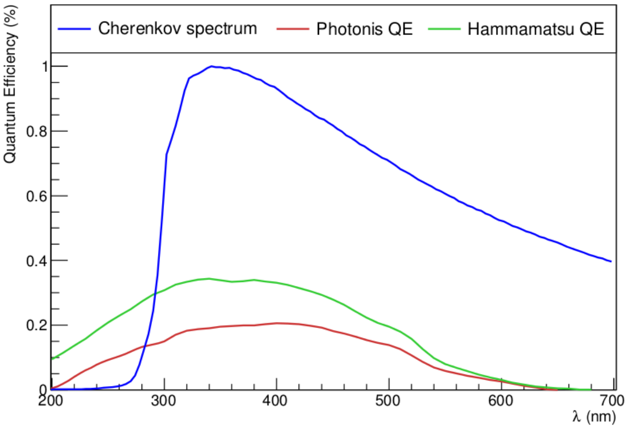

Figure 4–14: The QE over the optical light range for a Hamamatsu PMT as well as a Photonis PMT. The relative emission of Cherenkov light produced in a ∼500 GeV air shower is shown as well. The overall QE of the Hamamatsu PMTs is clearly greater than that of the Photonis specially near 350 nm where the Cherenkov spectrum peaks. Image source: figure 3-10 in [37].

A new calibration is necessary to measure the minimum sensitivity to optical flashes. The pixels' response to passing stars can be used to quantify their sensitivity. Calibration curves would need to be made for every season as the mirror reflectivity degrades over time. The typical read-out rate is increased thanks to the PMT upgrade; the L3 rate ranges from 300 to 400 Hz on an average night allowing better sampling for transients that are registered serendipitously during an air shower.

4.3.2 Flaring Red Dwarfs

In chapter 2 we discussed UV Ceti type stars that are dim and flare for a few minutes. The magnitude of these flares is within the limits of our methodology and their short timescale means that an entire flare can occur during a 20 minute exposure. Had a flare occurred during the archival search we performed it would not have been detected because we discounted channels that had stars crossing through them. A targeted archival search can be performed by selecting runs that saw red dwarfs in the FOV. A new trigger would be required to automatically detect flaring in a light curve. If observing time is available there is the opportunity for a dedicated search. The telescopes will track a star allowing the central channel to monitor flaring activity. A dedicated search would not require additional hardware but only that the read-out is triggered with a pulse generator to sample the flare at a consistent rate without having to depend on air showers setting the read-out. The array trigger can be activated externally at a fixed rate, this has already been done in the past to measure the throughput of Telescope 1 based on its central pixel's response to starlight [43].

4.3.3 Stellar Occultations

Small Transjovian Objects (TJOs) can be detected during stellar occultations. Occultation events by TJOs cast a diffraction pattern that can be observed with ground telescopes. As discussed in [21], the fluctuations in light level are small and shadows are cast for less than a second due to the relative speed of the TJO as seen on Earth. VERITAS offers fast sampling and sensitivity to stars of various magnitudes making it a good candidate for detecting TJOs. A simulated light curve is shown in Fig 4–15 for the occultation of a star with a V-band magnitude of 10. The signature of the occultation lasts less than 0.2 seconds. In order to detect occultations we would need a time resolution faster than a tenth of a second. Fast sampling of an occultation pattern can be achieved by tracking the star and a manual trigger.

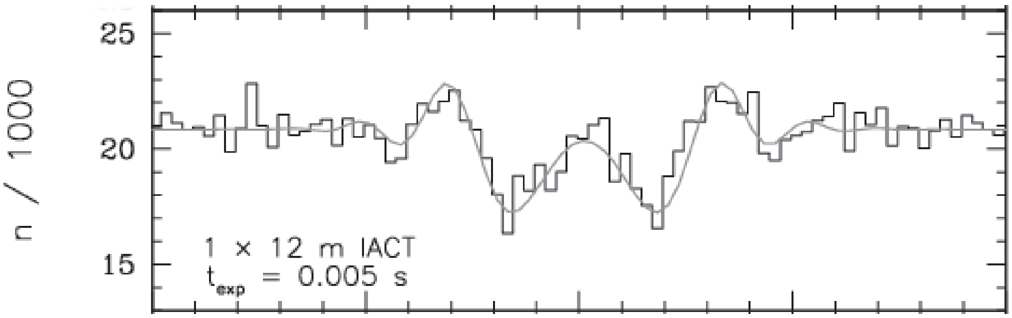

Figure 4–15: Simulated light curve of a stellar occultation event as seen by one pixel in a 12-meter IACT. The light level is measured in normalized photon counts with a time resolution of 0.005 seconds. An analogous light curve can be produced by VERITAS using variances provided the star is sufficiently bright. The time resolution can be achieved if the trigger is set with a pulse generator. Image source: adapted from figure 3 in [21].

CHAPTER 5
Conclusion

Imaging atmospheric Cherenkov telescopes are optical instruments designed to look for Cherenkov light so they have sub-second time resolution but lack the fine angular resolution of conventional telescopes. Their fast time resolution and large reflectors makes them fast and sensitive detectors of optical transients. We investigated how VERITAS fares at collecting background signals and used archival data to create proxy light curves with the Cherenkov foreground removed. We developed a methodology to search the light curves for transient signals and also use stars to obtain a calibration curve and determine the limiting sensitivity of the pixels. With this methodology we ran an analysis of V5 runs and found terrestrial transients crossing the cameras in timescales of 10^{-1} to 10 seconds. No astrophysical transients were found.

APPENDIX A
Calculating Variance, Mean, and Error

A.1 Calculating The Variance of a Distribution

Suppose we have a distribution of n samples $\{x_1, x_2, ..., x_n\}$. The variance of a distribution is the square of its standard deviation σ and is calculated as follows:

$$var = \sigma^2 = \frac{1}{n}\sum_{i=1}^{n}(x_i - \overline{x})^2, \tag{A.1}$$

where $\overline{x}$ is the mean of the distribution. As defined in [44], the uncertainty in the standard deviation $\delta\sigma$ of a set of samples taken from a Gaussian distribution is equal to $\sigma/\sqrt{2n}$ for large n. The uncertainty in the variance is

$$\delta\sigma^2 = 2\sigma\delta\sigma = 2\sigma\left(\frac{\sigma}{\sqrt{2n}}\right) = \sqrt{\frac{2}{n}}\sigma^2. \tag{A.2}$$

A.2 Calculating Mean and Uncertainty From a Distribution of Variances

For a set S_{total} of variances and their uncertainties, $S_{total} = \{\sigma_1^2 \pm \delta\sigma_1^2, \sigma_2^2 \pm \delta\sigma_2^2, ..., \sigma_{N_{total}}^2 \pm \delta\sigma_{N_{total}}^2\}$, we take subsets of three elements and pick the median of each subset. We create a new set S consisting of every median and its uncertainty, $S = \{\sigma_1^2 \pm \delta\sigma_1^2, \sigma_2^2 \pm \delta\sigma_2^2, ..., \sigma_{N_{median}}^2 \pm \delta\sigma_{N_{median}}^2\}$. Assuming that the distribution of variances is Gaussian we can calculate the mean σ_μ^2 of N variances using the following equation:

$$\sigma_\mu^2 = \frac{\sum_{i=1}^{N} \sigma_i^2/(\delta\sigma_i^2)^2}{\sum_{i=1}^{N} 1/(\delta\sigma_i^2)^2}. \tag{A.3}$$

Using equation (A.2) to expand $\delta\sigma_i^2$ we can simplify the above:

$$\sigma_\mu^2 = \frac{\sum_{i=1}^{N} \sigma_i^2/(\sqrt{\frac{2}{n}}\sigma_i^2)^2}{\sum_{i=1}^{N} 1/(\sqrt{\frac{2}{n}}\sigma_i^2)^2} = \frac{\sum_{i=1}^{N} 1/\sigma_i^2}{\sum_{i=1}^{N} 1/\sigma_i^4}. \tag{A.4}$$

The uncertainty in the mean is defined as

$$\delta\sigma_\mu^2 = \sqrt{\frac{1}{\sum_{i=1}^{N} 1/(\delta\sigma_i^2)^2}}, \tag{A.5}$$

substituting for $\delta\sigma_i^2$ gives

$$\delta\sigma_\mu^2 = \sqrt{\frac{1}{\sum_{i=1}^{N} 1/(\sqrt{\frac{2}{n}}\sigma_i^2)^2}} = \sqrt{\frac{2}{n\sum_{i=1}^{N} 1/\sigma_i^4}}. \tag{A.6}$$

References

[1] D. Morrison, S. Wolff, and A. Fraknoi. *Abell's exploration of the universe*. Lecture Notes in Mathematics. Saunders College Publishing, New York NY, 1995.

[2] B. E. Schaefer and A. C. Collazzi. "Novae with Long-lasting Supersoft Emission that Drive a High Accretion Rate". AJ, 139:1831–1843, May 2010.

[3] N. M. Law, S. R. Kulkarni, R. G. Dekany, E. O. Ofek, R. M. Quimby, P. E. Nugent, J. Surace, C. C. Grillmair, J. S. Bloom, M. M. Kasliwal, L. Bildsten, T. Brown, S. B. Cenko, D. Ciardi, E. Croner, S. G. Djorgovski, J. van Eyken, A. V. Filippenko, D. B. Fox, A. Gal-Yam, D. Hale, N. Hamam, G. Helou, J. Henning, D. A. Howell, J. Jacobsen, R. Laher, S. Mattingly, D. McKenna, A. Pickles, D. Poznanski, G. Rahmer, A. Rau, W. Rosing, M. Shara, R. Smith, D. Starr, M. Sullivan, V. Velur, R. Walters, and J. Zolkower. "The Palomar Transient Factory: System Overview, Performance, and First Results". PASP, 121:1395, December 2009.

[4] Palomar Observatory. "Supernovae PTF09atu, PTF09cnd, PTF09cwl, and PTF10cwr". `https://www.ptf.caltech.edu/image/ptf110608i`. Accessed: 2017-09-30.

[5] Arne Rau, Shrinivas R Kulkarni, Nicholas M Law, Joshua S Bloom, David Ciardi, George S Djorgovski, Derek B Fox, Avishay Gal-Yam, Carl C Grillmair, Mansi M Kasliwal, et al. "exploring the optical transient sky with the palomar transient factory". *Publications of the Astronomical Society of the Pacific*, 121(886):1334, 2009.

[6] X.-G. Wang, E.-W. Liang, L. Li, R.-J. Lu, J.-Y. Wei, and B. Zhang. "A Comprehensive Study of Gamma-Ray Burst Optical Emission. III. Brightness Distributions and Luminosity Functions of Optical Afterglows". ApJ, 774:132, September 2013.

[7] N. Gehrels. "The Swift Gamma-Ray Burst Mission". In E. Fenimore and M. Galassi, editors, *Gamma-Ray Bursts: 30 Years of Discovery*, volume 727

of *American Institute of Physics Conference Series*, pages 637–641, September 2004.

[8] J. S. Bloom, D. A. Perley, W. Li, N. R. Butler, A. A. Miller, D. Kocevski, D. A. Kann, R. J. Foley, H.-W. Chen, A. V. Filippenko, D. L. Starr, B. Macomber, J. X. Prochaska, R. Chornock, D. Poznanski, S. Klose, M. F. Skrutskie, S. Lopez, P. Hall, K. Glazebrook, and C. H. Blake. "Observations of the Naked-Eye GRB 080319B: Implications of Nature's Brightest Explosion". ApJ, 691:723–737, January 2009.

[9] D. R. Lorimer, M. Bailes, M. A. McLaughlin, D. J. Narkevic, and F. Crawford. "A Bright Millisecond Radio Burst of Extragalactic Origin". *Science*, 318:777, November 2007.

[10] A. Jessner, A. Słowikowska, B. Klein, H. Lesch, C. H. Jaroschek, G. Kanbach, and T. H. Hankins. "Giant radio pulses from the Crab pulsar". *Advances in Space Research*, 35:1166–1171, 2005.

[11] LG. "Spitler, P. Scholz, JWT. Hessels, S. Bogdanov, A. Brazier, F. Camilo, S. Chatterjee, JM. Cordes, F. Crawford, J. Deneva, and others". A repeating fast radio burst. *Nature*, 531(7593):202–205, 2016.

[12] P. Scholz, L. G. Spitler, J. W. T. Hessels, S. Chatterjee, J. M. Cordes, V. M. Kaspi, R. S. Wharton, C. G. Bassa, S. Bogdanov, F. Camilo, F. Crawford, J. Deneva, J. van Leeuwen, R. Lynch, E. C. Madsen, M. A. McLaughlin, M. Mickaliger, E. Parent, C. Patel, S. M. Ransom, A. Seymour, I. H. Stairs, B. W. Stappers, and S. P. Tendulkar. "The Repeating Fast Radio Burst FRB 121102: Multi-wavelength Observations and Additional Bursts". ApJ, 833:177, December 2016.

[13] V. Gajjar, A. P. V. Siemion, D. H. E. MacMahon, S. Croft, G. Hellbourg, H. Isaacson, J. E. Enriquez, D. C. Price, M. Lebofsky, D. DeBoer, D. Werthimer, J. Hickish, C. Brinkman, S. Chatterjee, and S. Ransom. "FRB 121102: Detection at 4 - 8 GHz band with Breakthrough Listen backend at Green Bank". *The Astronomer's Telegram*, 10675, August 2017.

[14] M. Lyutikov and D. R. Lorimer. "How Else Can We Detect Fast Radio Bursts?". ApJ, 824:L18, June 2016.

[15] VF. Shvartsman, GM. Beskin, RE. Gershberg, VL. Plakhotnichenko, and LA. Pustilnik. “minimum rise times in uv-ceti type flares”. *Soviet Astronomy Letters*, 14:97, 1988.

[16] H. A. Dal and S. Evren. “The statistical analyses of flares detected in B band photometry of UV Ceti type stars”. *New Astronomy*, 17:399–410, May 2012.

[17] G. M. Beskin, S. N. Mitronova, S. I. Neizvestny, V. L. Plokhotnichenko, M. Y. Popova, A. V. Zhuravkov, C. Bartolini, A. Guarnieri, R. Minarini, A. Piccioni, O. G. Benvenuto, C. Feinstein, and M. Mendez. “Photometric investigations of low-mass X-ray binaries with high time resolution”. *Astronomical and Astrophysical Transactions*, 13:273–281, 1997.

[18] M. B. Peacock, T. J. Maccarone, A. Kundu, and S. E. Zepf. “A systematic study of low-mass X-ray binaries in the M31 globular cluster system”. MNRAS, 407:2611–2624, October 2010.

[19] J.-P. Beaulieu, D. P. Bennett, P. Fouqué, A. Williams, M. Dominik, U. G. Jørgensen, D. Kubas, A. Cassan, C. Coutures, J. Greenhill, K. Hill, J. Menzies, P. D. Sackett, M. Albrow, S. Brillant, J. A. R. Caldwell, J. J. Calitz, K. H. Cook, E. Corrales, M. Desort, S. Dieters, D. Dominis, J. Donatowicz, M. Hoffman, S. Kane, J.-B. Marquette, R. Martin, P. Meintjes, K. Pollard, K. Sahu, C. Vinter, J. Wambsganss, K. Woller, K. Horne, I. Steele, D. M. Bramich, M. Burgdorf, C. Snodgrass, M. Bode, A. Udalski, M. K. Szymański, M. Kubiak, T. Więckowski, G. Pietrzyński, I. Soszyński, O. Szewczyk, Ł. Wyrzykowski, B. Paczyński, F. Abe, I. A. Bond, T. R. Britton, A. C. Gilmore, J. B. Hearnshaw, Y. Itow, K. Kamiya, P. M. Kilmartin, A. V. Korpela, K. Masuda, Y. Matsubara, M. Motomura, Y. Muraki, S. Nakamura, C. Okada, K. Ohnishi, N. J. Rattenbury, T. Sako, S. Sato, M. Sasaki, T. Sekiguchi, D. J. Sullivan, P. J. Tristram, P. C. M. Yock, and T. Yoshioka. “Discovery of a cool planet of 5.5 Earth masses through gravitational microlensing”. Nature, 439:437–440, January 2006.

[20] C. Mackay, M. Dominik, and I. Steele. “GravityCam: Higher Resolution Visible Wide-Field Imaging”. *ArXiv e-prints*, August 2016.

[21] B. C. Lacki. “On the use of Cherenkov Telescopes for outer Solar system body occultations”. MNRAS, 445:1858–1877, December 2014.

[22] H. E. Schlichting, E. O. Ofek, M. Wenz, R. Sari, A. Gal-Yam, M. Livio, E. Nelan, and S. Zucker. “A single sub-kilometre Kuiper belt object from a stellar occultation in archival data”. Nature, 462:895–897, December 2009.

[23] H. E. Schlichting, E. O. Ofek, R. Sari, E. P. Nelan, A. Gal-Yam, M. Wenz, P. Muirhead, N. Javanfar, and M. Livio. “Measuring the Abundance of Sub-kilometer-sized Kuiper Belt Objects Using Stellar Occultations”. ApJ, 761:150, December 2012.

[24] G. Benedict. *“Astrometry with Hubble Space Telescope”.* Groves Dictionaries Incorporated, November 2000.

[25] J. M. Madiedo, J. L. Ortiz, J. M. Trigo-Rodriguez, N. Konovalova, A. J. Castro-Tirado, and J. Cabrera-Caño. “Two Superbolides with a Cometary Origin Observed over the Iberian Peninsula”. *European Planetary Science Congress*, 8:EPSC2013–260, September 2013.

[26] S. Karpov, G. Beskin, S. Bondar, A. Guarnieri, C. Bartolini, G. Greco, and A. Piccioni. “wide and fast: Monitoring the sky in subsecond domain with the favor and tortora cameras”. *Advances in Astronomy*, 2010, 2010.

[27] G. Greco, G. Beskin, S. Karpov, A. Guarnieri, C. Bartolini, S. Bondar, A. Piccioni, and E. Molinari. “The High-Speed and Wide-Field TORTORA Camera: description & results.”. *Memorie della Societa Astronomica Italiana Supplementi*, 14:267, 2010.

[28] T. Hassan, J. Hoang, M. López, J. A. Barrio, J. Cortina, D. Fidalgo, D. Fink, L. A. Tejedor, and M. Will. “MAGIC sensitivity to millisecond-duration optical pulses”. *ArXiv e-prints*, August 2017.

[29] C. Deil, W. Domainko, G. Hermann, A. C. Clapson, A. Förster, C. van Eldik, and W. Hofmann. “Capability of Cherenkov telescopes to observe ultra-fast optical flares”. *Astroparticle Physics*, 31:156–162, March 2009.

[30] S. Griffin. “searching for fast optical transients using a veritas cherenkov telescope”. volume 7, pages 321–323. Cambridge Univ Press, 2011.

[31] A. U. Abeysekara, S. Archambault, A. Archer, W. Benbow, R. Bird, M. Buchovecky, J. H. Buckley, K. Byrum, J. V. Cardenzana, M. Cerruti, X. Chen, J. L. Christiansen, L. Ciupik, W. Cui, H. J. Dickinson, J. D. Eisch, M. Errando,

A. Falcone, D. J. Fegan, Q. Feng, J. P. Finley, H. Fleischhack, P. Fortin, L. Fortson, A. Furniss, G. H. Gillanders, S. Griffin, J. Grube, G. Gyuk, M. Hütten, N. Håkansson, D. Hanna, J. Holder, T. B. Humensky, C. A. Johnson, P. Kaaret, P. Kar, N. Kelley-Hoskins, M. Kertzman, D. Kieda, M. Krause, F. Krennrich, S. Kumar, M. J. Lang, T. T. Y. Lin, G. Maier, S. McArthur, A. McCann, K. Meagher, P. Moriarty, R. Mukherjee, D. Nieto, S. O'Brien, A. O'Faoláin de Bhróithe, R. A. Ong, A. N. Otte, N. Park, J. S. Perkins, A. Petrashyk, M. Pohl, A. Popkow, E. Pueschel, J. Quinn, K. Ragan, G. Ratliff, P. T. Reynolds, G. T. Richards, E. Roache, M. Santander, G. H. Sembroski, K. Shahinyan, D. Staszak, I. Telezhinsky, J. V. Tucci, J. Tyler, S. Vincent, S. P. Wakely, O. M. Weiner, A. Weinstein, D. A. Williams, and B. Zitzer. "A Search for Brief Optical Flashes Associated with the SETI Target KIC 8462852". ApJ, 818:L33, February 2016.

[32] J. Holder, R. W. Atkins, H. M. Badran, G. Blaylock, S. M. Bradbury, J. H. Buckley, K. L. Byrum, D. A. Carter-Lewis, O. Celik, Y. C. K. Chow, P. Cogan, W. Cui, M. K. Daniel, I. de la Calle Perez, C. Dowdall, P. Dowkontt, C. Duke, A. D. Falcone, S. J. Fegan, J. P. Finley, P. Fortin, L. F. Fortson, K. Gibbs, G. Gillanders, O. J. Glidewell, J. Grube, K. J. Gutierrez, G. Gyuk, J. Hall, D. Hanna, E. Hays, D. Horan, S. B. Hughes, T. B. Humensky, A. Imran, I. Jung, P. Kaaret, G. E. Kenny, D. Kieda, J. Kildea, J. Knapp, H. Krawczynski, F. Krennrich, M. J. Lang, S. LeBohec, E. Linton, E. K. Little, G. Maier, H. Manseri, A. Milovanovic, P. Moriarty, R. Mukherjee, P. A. Ogden, R. A. Ong, D. Petry, J. S. Perkins, F. Pizlo, M. Pohl, J. Quinn, K. Ragan, P. T. Reynolds, E. T. Roache, H. J. Rose, M. Schroedter, G. H. Sembroski, G. Sleege, D. Steele, S. P. Swordy, A. Syson, J. A. Toner, L. Valcarcel, V. V. Vassiliev, S. P. Wakely, T. C. Weekes, R. J. White, D. A. Williams, and R. Wagner. "The first VERITAS telescope". *Astroparticle Physics*, 25:391–401, July 2006.

[33] R. Winston. "light collection within the framework of geometrical optics$*$". *J. Opt. Soc. Am.*, 60(2):245–247, Feb 1970.

[34] VERITAS Collaboration: T. Nagai, R. McKay, G. Sleege, and D. Petry. "Focal Plane Instrumentation of VERITAS". *ArXiv e-prints*, September 2007.

[35] A. Nepomuk Otte and for the VERITAS Collaboration. "The Upgrade of VERITAS with High Efficiency Photomultipliers". *ArXiv e-prints*, October 2011.

[36] Hamamatsu. "Photomultiplier tubes basics and applications". `https://www.hamamatsu.com/resources/pdf/etd/PMT_handbook_v3aE.pdf`. Accessed: 2017-09-30.

[37] S. Griffin. *"The VERITAS Bright Moonlight Program"*. PhD thesis, McGill University, 2016.

[38] A. McCann, D. Hanna, J. Kildea, and M. McCutcheon. "A new mirror alignment system for the VERITAS telescopes". *Astroparticle Physics*, 32:325–329, January 2010.

[39] A. MacLeod. "Measuring the Gain of a Photomultiplier Tube". Master's thesis, McGill University, 2007.

[40] David Hanna. "Looking for Optical Transients with the VERITAS Telescopes". 2006 (unpublished article).

[41] M. Wenger, F. Ochsenbein, D. Egret, P. Dubois, F. Bonnarel, S. Borde, F. Genova, G. Jasniewicz, S. Laloë, S. Lesteven, and R. Monier. "The SIMBAD astronomical database. The CDS reference database for astronomical objects". 143:9–22, April 2000.

[42] Petrov, G. "Lectures on Astronomy- after Hawley J.F. (1999)". `http://astro.bas.bg/~petrov/hawley99.html`. Accessed: 2017-09-30.

[43] S. Griffin and D. Hanna. "Using Raster Scans of Bright Stars to Measure the Relative Total Throughputs of Cherenkov Telescopes". *ArXiv e-prints 1307.8355*, July 2013.

[44] K. A. Olive et al. "Review of Particle Physics". *Chin. Phys.*, C38:090001, 2014.